Archives of Computational Methods in Engineering (2025) 32:1969–1995
https://doi.org/10.1007/s11831-024-10198-0

REVIEW

State-of-the-Art Review of Continuum Mechanics-Based Modelling of Soil Surface Erosion

Hang Feng[1] · Zhen-Yu Yin[1,2] · Maozhu Peng[1] · Qimeng Guo[1]

Received: 10 May 2024 / Accepted: 17 October 2024 / Published online: 5 November 2024

Abstract
Soil surface erosion can shape the morphography of rivers and estuaries in the natural environment and induce high potential risks to structures in engineering. Numerical simulations based on continuum mechanics theory can provide reliable assessments of the evolution of surface erosion from the perspective of a large-scale view. However, current studies on continuum mechanics-based modelling are still limited. This paper comprehensively reviews such numerical simulations of soil surface erosion. This review begins by discussing the fundamental physical mechanisms of surface erosion. Subsequently, it explores the basic physics-based conservation equations controlling soils and fluids in surface erosion. Then, the empirical formulae depicting the different stages of surface erosion are presented. Building on these mathematical foundations, this paper reviews various numerical methods for surface erosion modelling from a continuum mechanics perspective. Finally, this paper discusses the advantages and limitations of the numerical methods. This work can provide researchers convenience for using numerical models on surface erosion simulations.

1 Introduction

Soil erosion is a process in which flow water flow carries soil particles away. It is generally divided into internal erosion occurring inside the soil (refer to [1–4]) and surface erosion happening at the surface of the soil [5–7]. This process differs for sands and clays due to their different permeability properties. Non-cohesive soils are generally more vulnerable to surface erosion compared to cohesive soils [8–10]. Accordingly, this paper mainly focuses on the surface erosion of non-cohesionless soils.

In the natural environment and engineering field, various macro phenomena (e.g., riverbed erosion, beach erosion, overtopping, and local scour) (see Fig. 1) are associated with surface erosion.

These phenomena can be briefly described as follows: (i) Riverbed erosion (see Fig. 1a): Also known as sediment transport in river hydraulics, which has created the morphography of rivers and estuaries in the natural environment. (ii) Beach erosion (see Fig. 1b): This occurs on beaches and plays a crucial role in shaping shoreline configurations [11]. (iii) Local scour (see Fig. 1c): in local scour, the flow is obstructed by structures, which leads to the increased flow velocity to bring soil particles away. It can induce instability of the foundation in offshore geotechnical engineering or bridge engineering [8, 12–18]. According to the National Cooperative Highway Research Program (NCHRP) of the United States [19], over 800 bridge failures from 1996 to 2005 were attributed to the hydraulic erosion problem and insufficient scour protection (see Fig. 2). And the foundation design code [20] also emphasises the significance of estimating local scour. (iv) Overtopping (see Fig. 1d): Commonly observed in dams (e.g., the earth dam, tailing deposition embankment, and landslide dam) where the downstream flow brings soil particles away. It is reported that more than one-third of dam failures were caused due to overtopping [21, 22]. Additionally, over 90% of the recorded landslide dam failures were induced by overtopping [23]. Given the impact posed by surface erosion on the natural environment, there is an urgent need for an accurate estimation of the evolution of surface erosion.

Accurate estimation of these macro phenomena requires a comprehensive understanding of the physical mechanism of surface erosion (see Fig. 1e, f). In recent years, many

✉ Zhen-Yu Yin
zhenyu.yin@polyu.edu.hk

[1] Department of Civil and Environmental Engineering, The Hong Kong Polytechnic University, Hong Kong, China

[2] Research Centre for Nature-based Urban Infrastructure Solutions, The Hong Kong Polytechnic University, Hong Kong, China

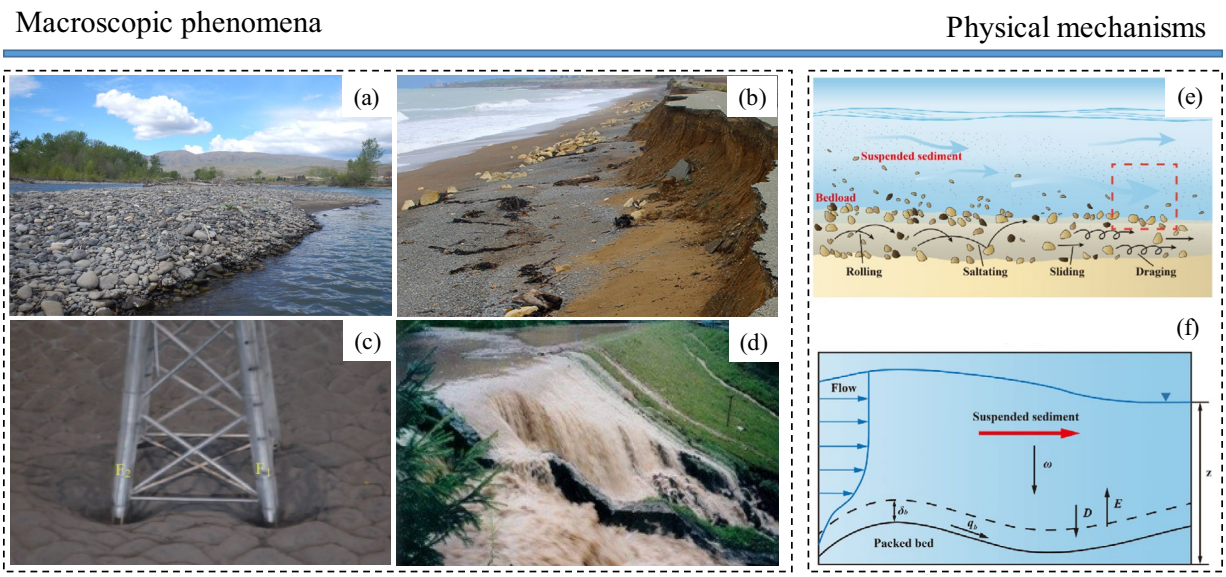

Fig. 1 Macroscopic phenomena with surface erosion: (**a**) Riverbed erosion (https://nhcweb.com/projects/naches-river-morphodynamics-and-sediment-transport-study/); (**b**) Beach erosion (https://damfailures.org/wp-content/uploads/2015/07/Design-Flood-2.jpg); (**c**) Local scour [192], (**d**) Overtopping [193], (**e**) Movement of soil particles during surface erosion [23] (**f**) The mechanism depicting the evolution of surface erosion [23]

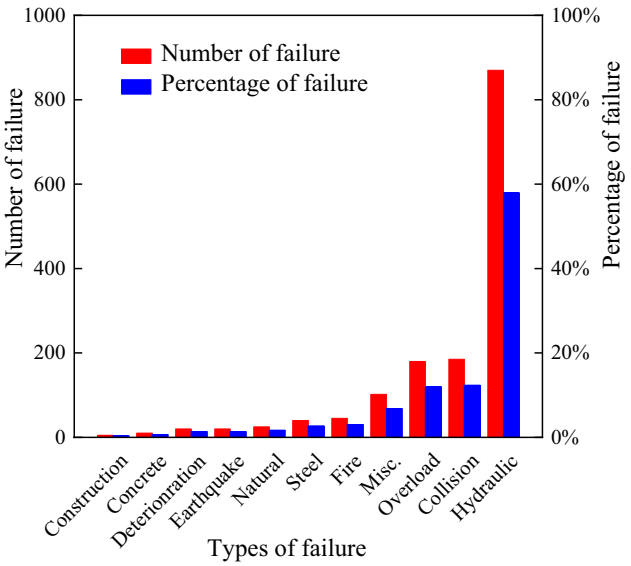

Fig. 2 Number of bridge failures from 1996 to 2005 (total 1502) in USA [19]

studies (e.g., [24–32]) have adopted experimental methods to investigate surface erosion. These experiments have successfully unveiled some fundamental mechanisms of surface erosion and provided practical formulae for predicting the evolution process of surface erosion. However, experimental investigations face challenges, such as the inability to replicate the influence of real water depth [33–35]. Alternatively, numerical modelling, due to advantages such as cost-effectiveness, accessibility to challenging environments, and repeatability, turns out to be a good complement.

Currently, numerical simulations on surface erosion mainly rely on the non-continuum and continuum mechanics. The former is primarily achieved through methods such as the discrete element method (i.e., DEM) (e.g., [36–41]), and is applicable at microscopic or mesoscopic scales. While the latter often employed methods such as the finite element method and finite volume method, are well-suited for solving large-scale problems (refer to [33–35, 42–49]). For a typical boundary value problem like surface erosion, continuum mechanics-based approaches appear to be an advantageous choice to provide large-scale estimation in the engineering field. As a result, this paper aims to give a comprehensive review of surface erosion simulation based on continuum mechanics. Through this review, we provide insights into the basic mechanisms of surface erosion, mathematical equations depicting these mechanisms, and the continuum mechanics-based numerical approaches to solve these mathematical equations.

Figure 3 shows the framework of this review: Sect. 2 gives a basic understanding of the physical process of surface erosion. Section 3 discusses the soil, hydraulic, and structure conditions during surface erosion. Section 4 describes fundamental mass and momentum conservation equations for the soils and hydraulic conditions, followed by Sect. 5, which presents empirical formulae describing the various stages of erosion. Section 6 presents available continuum mechanics-based numerical approaches to solving prescribed mathematical equations. In Sect. 7, we discuss

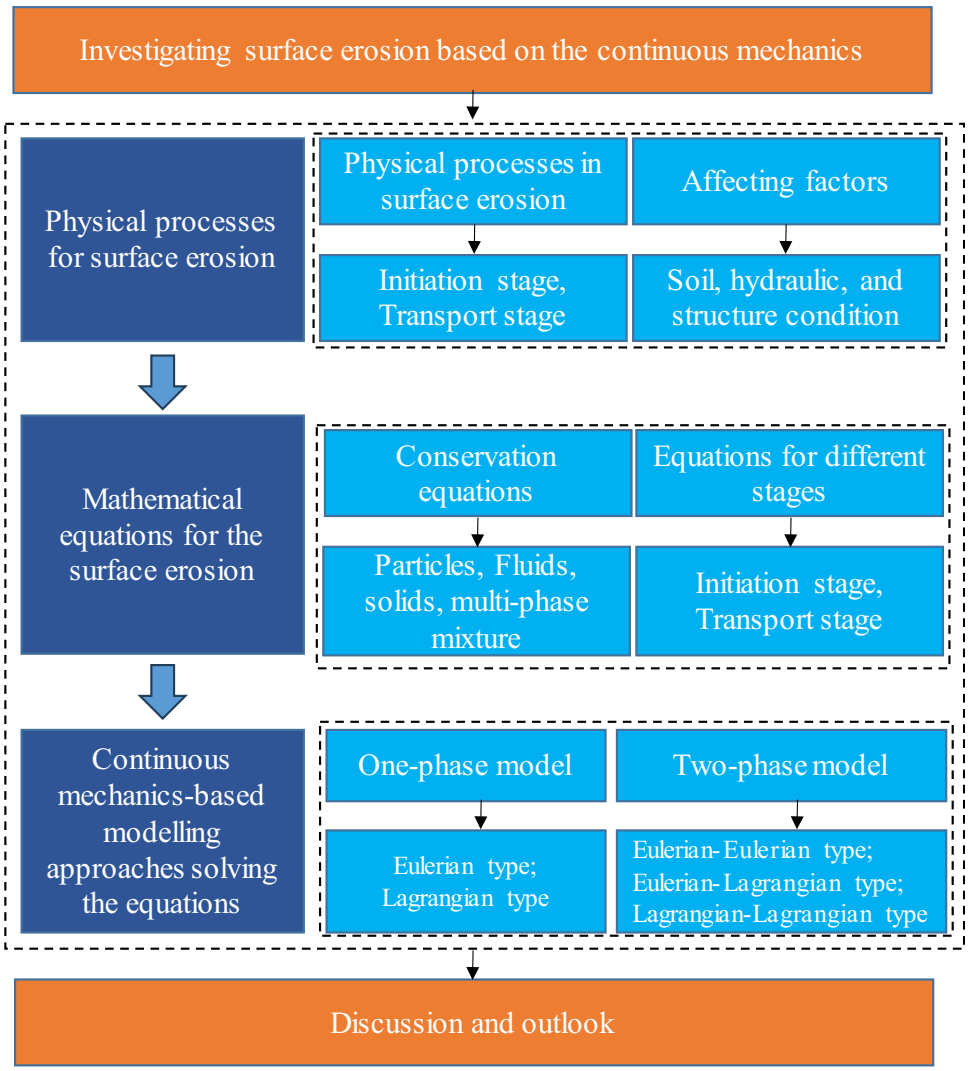

Fig. 3 Overall framework for this review

the limitations and challenges of surface erosion simulation approaches. The review concludes with Sect. 8.

2 Physical Process of Surface Erosion

Understanding the basic physical process of surface erosion is fundamental to establishing adequate mathematical equations for a realistic numerical simulation. Accordingly, this section comprehensively reviews the fundamental mechanisms underlying surface erosion.

2.1 Initiation Stage

The surface erosion process, i.e., the movement of soil particles due to the flow, can be divided into three stages: initiation, transport, and sedimentation [6].

The initiation stage of surface erosion marks the onset of particle movement, a stage intricately linked to the equilibrium between the hydraulic forces and the resisting forces (e.g., due to interparticle interactions) acting on a particle. Surface erosion is triggered once the former overcomes the latter [50]. This process is highly complex, mainly influenced by hydraulic conditions and soil properties, because hydraulic conditions (e.g., laminar or turbulent flow conditions) determine hydraulic forces acting on the particle and soil properties can affect the intergranular interactions, primarily particle collisions for sands. It is worth noting that the non-uniformity of soils makes the initiation a stochastic process [51]. Especially under complex turbulent flow conditions, this stochastic initiation may involve simultaneous initiation of large and small particles or a sequential initiation where small particles move before large particles [51].

The momentum conservation equation Eq. (1), which describes the equilibrium of soil particles in flow, can be utilised.

$$m_p \frac{\partial u_p}{\partial t} = m_p g + F_f + F_p \tag{1}$$

where m_p denotes the mass of the particle; u_p is the velocity of the particle; F_f and F_p represent the overall particle–fluid interaction force and particle–particle interaction force (i.e., both are surface forces acting on the particle), respectively.

The particle–particle interaction force F_p is generated once the particle contacts other particles. The particle–fluid interaction forces significantly influence particle movement [52–54]. As is shown in Fig. 4, different particle–fluid forces have been considered in existing literature for laminar flow conditions, including drag force, pressure gradient force, virtual mass force, Basset force, Saffman force, and Magnus force. Among them, the drag force and pressure gradient force are significant in particle–fluid interactions. The virtual mass force and Basset force are related to the acceleration or deceleration of the particle. The Saffman force and Mgnus force are typically lift forces for the particle.

The drag force is generated by the relative velocity between the particle and fluid, which mainly contributes to particle kinematics. It can be calculated using the following widely accepted equation [52]:

$$F_{\text{drag}} = \beta_{\text{drag}} \left(u_f - u_p\right) \tag{2}$$

where u_f and u_p denote the velocity of the fluid and particle, respectively; β_{drag} is the coefficient representing the momentum transfer between the particle and fluid. One equation for the coefficient β_{drag} is expressed as $\frac{1}{2} C_d A_P \rho_f \left|u_f - u_p\right|$ [55], in which C_d denotes the dimensionless drag coefficient, a parameter that varies with Reynolds number R_e, A_{P} is the projected area of the particle in the flow direction (calculated as $\pi d^2/4$); ρ_f is the density of the fluid. Note that the drag coefficient C_d can be estimated by many empirical formulae in existing studies (Detailed formulae can be found in Zhao et al. [54]).

The pressure gradient force is due to the pressure gradient in the flow field, which is expressed by:

$$F_{\nabla p} = -V_p \nabla p \tag{3}$$

where V_p is the volume of the particle. ∇p is the total flow pressure gradient consisting of the hydrostatic and hydrodynamic parts, and the hydrostatic part in Eq. (3) represents the buoyancy force. Idealising the soil particle into a sphere, the submerged weight F_G can be obtained as:

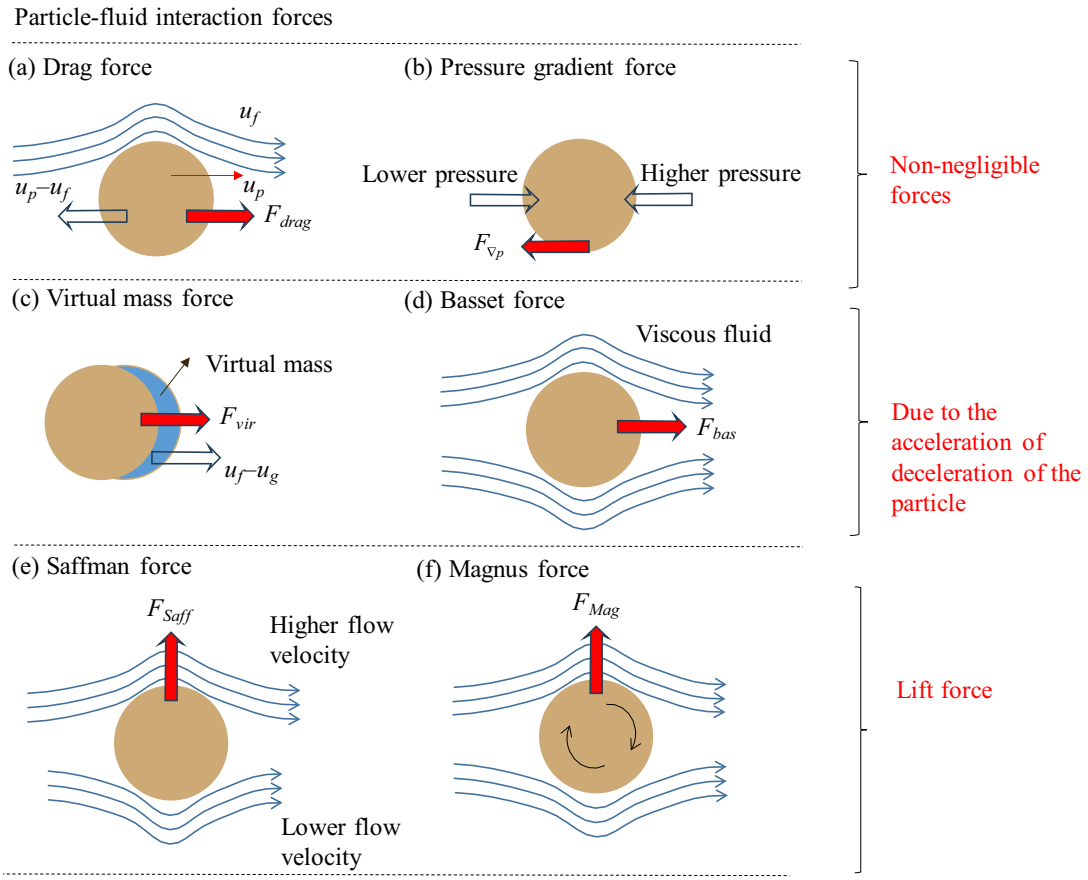

Fig. 4 The schematic diagram of particle–fluid interaction forces

$$F_G = \frac{1}{6}\pi d^3\left(\gamma_p - \gamma_f\right) \tag{4}$$

where d is the diameter of the soil particle, γ_p and γ_f are the unit weight of the particle and fluid, respectively.

Detailed expressions for other forces are given in Table 1. Specifically, the virtual mass force is a result of the acceleration or deceleration of the particle: the particle experiencing the acceleration or deceleration will influence the state of the surrounding fluid, which can be regarded as a virtual additional mass for the particle (see Fig. 4c). The Basset force is generated due to the hysteresis phenomenon in the viscous fluid layer surrounding the particle. It considers the effect of the viscous fluid's history on the particle (also known as the history force) (see Fig. 4d). The Saffman lift force (1965) is a result of the pressure difference between opposite sides of the particle, corresponding to the velocity difference according to Bernoulli's principle (see Fig. 4e). The Magnus lift force is related to the Magnus effect: when the particle rotates in the flow field, it generates a lift force perpendicular to the direction of the flow field (see Fig. 4f).

In addition to the above particle–fluid interaction forces highly related to laminar flow conditions, turbulence also plays a crucial role in the initiation stage. As flow velocity increases and transitions to a turbulent regime, small eddies form around particles. The interaction of these turbulent vortices with the particle boundary reduces pressure on the boundary, resulting in a pressure difference across the particle. This pressure imbalance greatly adds to the initiation of erosion [56]. Consequently, the influence of small turbulent eddies must be accounted for when describing the initiation of particles in turbulent flows.

2.2 Transport Stage

Once the particles start moving, they can be transported via either the bed-load transport type or suspended-load

Table 1 Summary of particle–fluid interaction forces in the existing literature

Force	Equation	References
Drag force	$F_{\text{drag}} = \beta_{\text{drag}}\left(u_f - u_p\right)$ $\beta_{drag} = \frac{1}{2}C_d A_P \rho_f \left\lvert u_f - u_p \right\rvert$ C_d: the drag coefficient	Zhao et al. [54] Sun and Yu, [55]
Pressure gradient force	$F_{\nabla p} = -V_p \nabla p$	Zhao et al. [54]
Virtual mass force	$F_{vir} = C_{vir}\frac{\rho_f}{\rho_p} m_p\left(u_f - u_p\right)$ $C_{vir:}$ the correction factor	Zhao et al. [54]
Basset force	$F_{bas} = \frac{3}{2}d_p^2\sqrt{\rho_f \mu_f \pi}\int_0^t \frac{d(u_f - v_p)/d\tau_s}{\sqrt{t-\tau_s}}d\tau$ τ_s: the Stokes relaxation time	Reeks and Mckee [196]
Saffman force	$F_{Saf} = C_L\sqrt{\rho_f \mu_f} d^2\left(u_f - u_p\right) \times (\nabla \times u)\lvert\nabla \times u\rvert^{-0.5}$ C_L: the Saffman force coefficient	Saffman [197] Harris and Davidson, [104]
Magnus force	$F_{\text{Mag}} = \frac{\pi}{8}d^3\rho_{\text{f}}[(\frac{1}{2}\nabla \times u_{\text{f}} - \omega_{\text{p}}) \times (u_{\text{f}} - u_{\text{p}})]$	Crowe et al. [77] Nasrollahi et al. [99]

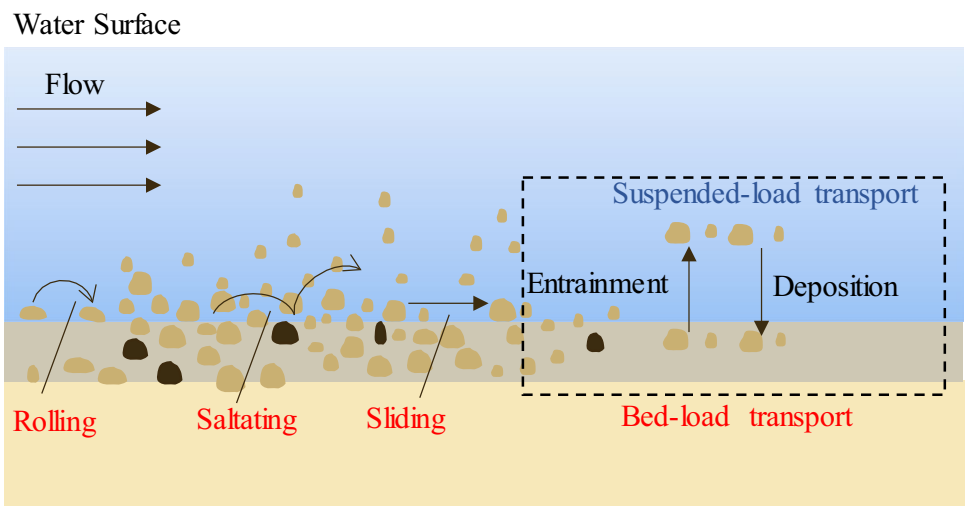

Fig. 5 The bed-load transport and suspended-load transport in surface erosion

transport type, depending on the hydraulic condition (see Fig. 5). Bed-load transport describes particles transport along the mudline through processes such as rolling, sliding, and saltating. In contrast, suspended-load transport refers to the particles entering the fluid medium and remaining suspended in the flow [6, 51, 57]. Particles transported via the bed-load type contribute 5–10% of the total sediment transport in a stream [6], indicating that a notable proportion of soil particles detach from the surface into the fluid.

The bed-load and suspended-load transport undergo transitions between each other as flow conditions change [6, 18, 23]. Bed-load transport particles can shift into the suspended-load type when the upward hydraulic force acting on a particle becomes dominant in the vertical direction among other forces, a phenomenon known as suspension or entrainment. Conversely, as the flow velocity decreases, gravity becomes dominant in the vertical direction, and suspended-load transport particles settle back to the riverbed in a process known as deposition. Eventually, these settled particles become static again, marking the end of their journey in the ocean (i.e., the sedimentation stage).

3 Important Factors in Surface Erosion

Three main factors, including the soil, hydraulic and structure conditions, should be considered in simulating the physical process discussed in Sects. 2.1 and 2.2.

3.1 Soil Condition

Figure 6 simplifies the complex surface erosion process by assuming a horizontal mudline. At the same time, some soil particles are eroded from the soil layer while other particles settle down, resulting in an eroded surface (i.e., the upper bound of the soil layer and the bottom bound of the fluid layer). In addition, there is a small portion of erodible particles that have not yet detached the mudline and a significant amount of non-erodible particles which contribute intergranular forces to the erodible particles to prevent them from erosion. Note that non-erodible particles may experience disturbance due to possible changes in the stress history [58, 59, 59].

3.2 Hydraulic Condition

The primary considerations of the hydraulic condition in surface erosion include currents and waves [8, 60–62]. Currents refer to the flow of water in a specific direction, while waves are defined as disturbances travelling inside the fluid, usually occurring at the water–air interface. Currents are generally described by a constant flow velocity, while waves are usually characterised by the wavelength, frequency, and amplitude. Waves can make the riverbed susceptible to suspension by providing a strong periodic drag force [8]. It is worth noting that the current-wave coupling conditions are more common in practical conditions. A detailed description of fluid conditions influencing surface erosion can be found in Li et al. [8]. To consider the hydraulic condition, theoretical conservation equations based on continuum mechanics are the prevalent choice in existing studies (refer to Sect. 4).

3.3 Structure Condition

The presence of structures can affect the erosion process, where the structures mainly are marine pipelines,

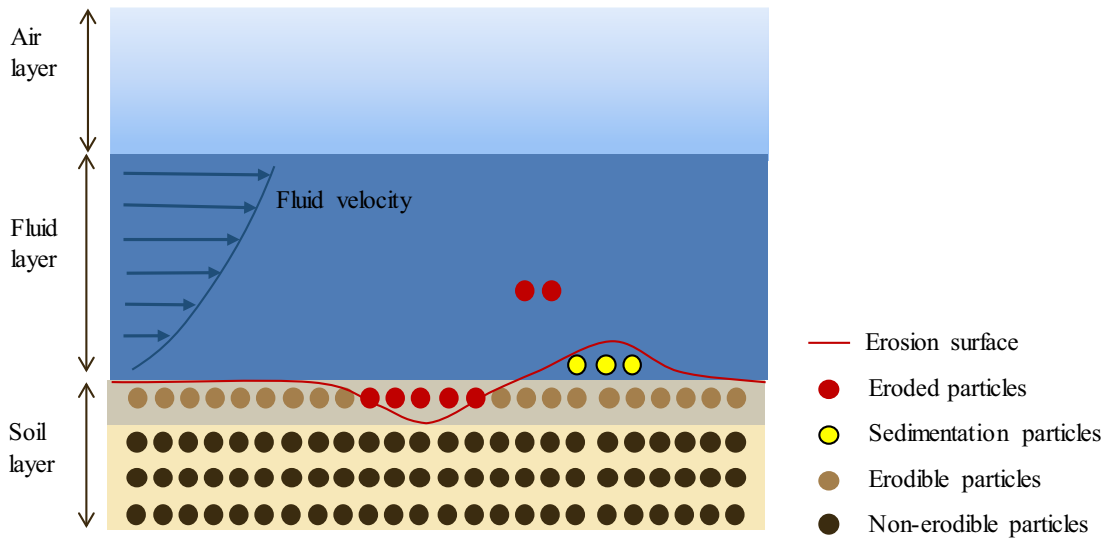

Fig. 6 Different soil particles during surface erosion

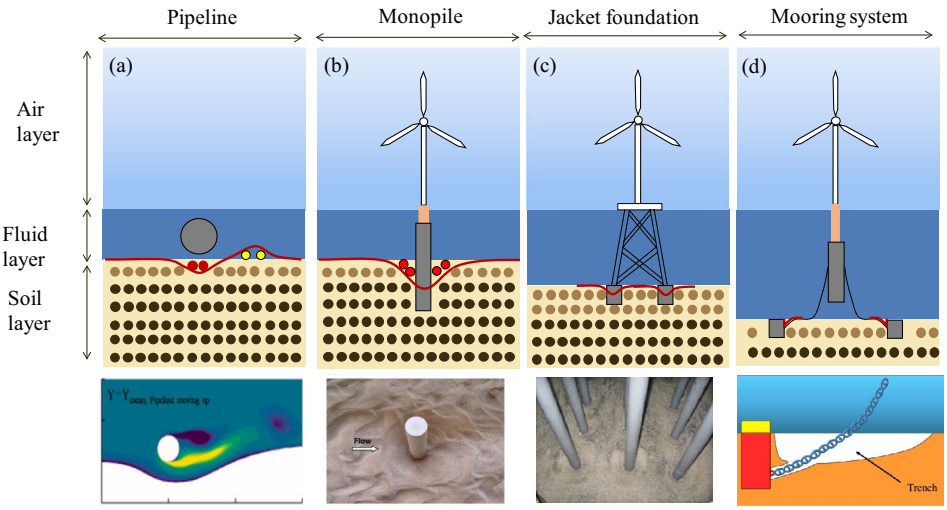

Fig. 7 Surface erosion with different structures [44, 191, 194, 195]

foundations (e.g., the suction caisson, monopile, and jacket foundation), and mooring system, as is shown in Fig. 7. The behaviours of surface erosion with different structures are described as:

(a) Pipelines and fixed foundations (see Fig. 7a–c): When the flow is disturbed by the structures, three types of flow were identified: (i) downward flow in front of the structure; (ii) the horseshoe vortex in front of the structure base; (iii) the vortex at the back of the structure [8, 14, 18]. These different types of flow play a significant role in the formation of scour holes [8, 18]. Note that pipeline spans may experience vortex-induced vibration (VIV), which induces a deeper erosion hole than the fixed pipe [63].
(b) Mooring system (see Fig. 7d): the mooring line linking upper floating structures and lower anchors is seen as a dynamic structure because the floating structure drives the mooring line to move back and forth in large amplitude [64]. The mooring line repeatedly cuts into the seabed and simultaneously induces current turbulence near the seabed, leading to the formation of seabed trenches (see Fig. 7d).

4 Physics-Based Mathematical Model

Mathematical models depicting surface erosion can be categorised into physics-based and empiricism-based mathematical models. The former essentially refers to the mass and momentum conservation equations of soils and fluids, while most equations in the latter are empirical to depict the initiation and transport stages of surface erosion (in Sect. 5). We will focus on physics-based governing equations for soils and fluids in this section.

At the macroscale, various mathematical models are employed to describe soils and fluids in surface erosion in existing literature, as illustrated in Fig. 8. Some studies adopt equations tailored for one-phase media, i.e., using one-phase solid media to represent soils and treating fluid conditions as one-phase flow. However, a more effective approach is treating soils in the ocean as saturated porous media consisting of the solid skeleton and pore fluid. Additionally, the hydraulic condition is frequently modelled as a two-phase flow media, incorporating eroded solid particles carried by the water flow. The two-phase flow and saturated porous media can be seen as a multiphase mixture in existing literature.

4.1 Equations for One-Phase Media

4.1.1 Equations for Fluids as Single-Phase Flow

In describing the behaviours of the fluids, the Navier–Stokes equations are the mainstream choice. However, when turbulent flows need to be considered, using NS equations can lead to an extensive computational burden. To overcome this difficulty, the Reynolds averaged Navier–Stokes equations, which first integrate the NS equations with respect to time and then average them against time, are usually adopted to save the computational cost (e.g., [33–35, 42–44, 46–49]). Due to the time-averaging operation, the number of unknown variables has increased to more than the number of equations. Thus, the RANS equations can only be solved by combining them with complementary turbulence models, such as the Spalart–Allmaras, k-ε, k-ω, and Reynolds stress model (RSM).

The RANS equations are given as:

$$\frac{\partial \rho}{\partial t} + \frac{\partial \rho u_i}{\partial x_i} = 0 \tag{5}$$

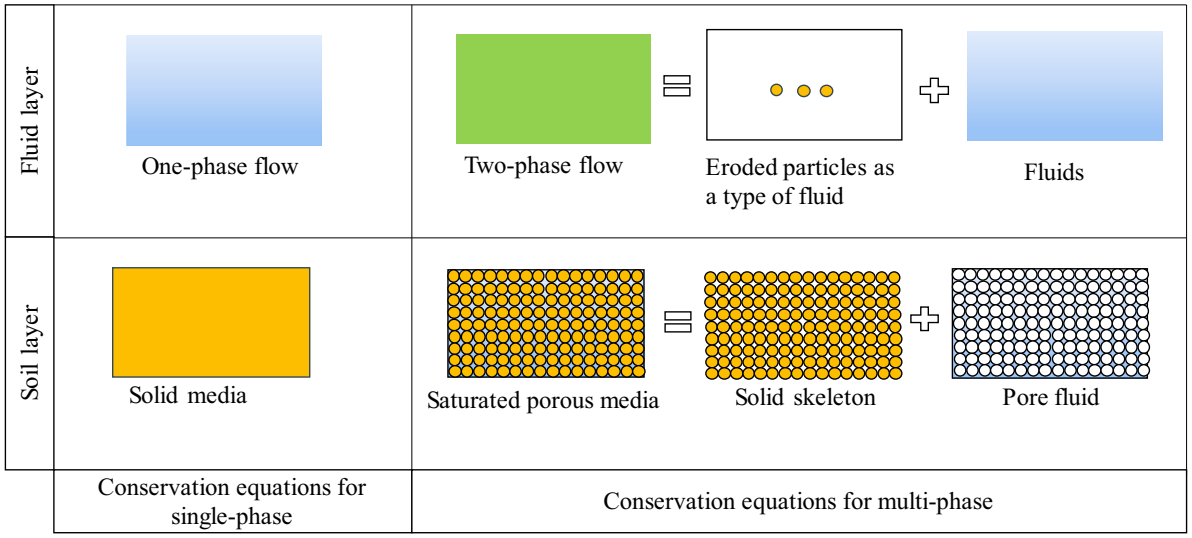

Fig. 8 Different treatments for soils and fluids at the macroscale

$$\frac{\partial u_i}{\partial t} + u_j \frac{\partial u_i}{\partial x_j} = -\frac{1}{\rho}\frac{\partial p}{\partial x_i} + \frac{\partial}{\partial x_j}\left[\nu\left(\frac{\partial u_i}{\partial x_j} + \frac{\partial u_j}{\partial x_i}\right) - \overline{u_i u_j}\right] + g_i \tag{6}$$

where u_i is the fluid velocity; p denotes the fluid pressure; ν is the kinematic viscosity; g is the gravitational acceleration; $\overline{u_i u_j}$ is the Reynolds stress, representing the influence of turbulent.

Following the Boussinesq-approximation [65, 66], the $\overline{u_i u_j}$ can be written as:

$$-\overline{u_i u_j} = \nu_t\left(\frac{\partial u_i}{\partial x_j} + \frac{\partial u_j}{\partial x_i}\right) + \frac{2}{3}k\delta_{ij} \tag{7}$$

where δ_{ij} is the Kronecker delta; ν_t is the eddy viscosity, which can be calculated by the k-ω model [67]:

$$\nu_t = k/\omega \tag{8}$$

$$\frac{\partial k}{\partial t} + u_j \frac{\partial k}{\partial x_j} = \frac{\partial}{\partial x_j}\left[\left(\nu + \frac{\nu_t}{\sigma_k}\right)\frac{\partial k}{\partial x_j}\right] + P_k - \beta_k k\omega \tag{9}$$

$$\frac{\partial \omega}{\partial t} + u_j \frac{\partial \omega}{\partial x_j} = \frac{\partial}{\partial x_j}\left[\left(\nu + \frac{\nu_t}{\sigma_\omega}\right)\frac{\partial \omega}{\partial x_j}\right] + \alpha\frac{\omega}{k}P_k - \beta\omega^2 \tag{10}$$

$$P_k = \nu_t \frac{\partial u_i}{\partial x_j}\left[\frac{\partial u_i}{\partial x_j} + \frac{\partial u_j}{\partial x_i}\right] \tag{11}$$

where k is the turbulent kinetic energy density; ω is the specific turbulent dissipation rate; P_k is the production of turbulent kinetic energy; Parameters σ_k and σ_ω represent the turbulent Prandtl number for kinetic energy and specific rate of dissipation, respectively; α is a model constant, determining the contribution of the production of turbulent kinetic energy P_k to the production of specific rate of dissipation; β represents the ratio of the production of ω due to the mean velocity gradients to the destruction of ω; β_k is a model constant associated with the pressure-strain correlation, detailed values of these parameters can found in Ahmad et al. [65].

4.1.2 Equations for Soils as Solids

The momentum conservation for solids can be expressed as Eq. (12). Note that this equation is more suitable for continuous material without porosity.

$$\frac{\partial \sigma_{ij}^s}{\partial x_j} + \rho_s g_i - \rho_s a_s = 0 \tag{12}$$

where ρ_s is the soil density, a_s is the acceleration of the solid, and g_i is the acceleration due to gravity. σ^s is total the soil stress tensor, which can be effectively expressed via the constitutive models (e.g., [68–73]) to reproduce the relationship between stress and strain.

4.2 Equations for Multi-Phase Mixture

Equation (1) explains the mechanics of surface erosion at particle scale. Equations (5, 6, 7, 8, 9, 10, 11) describe the behaviour of fluid without the disturbance of eroded particles. Equation (12) explains the behaviour of solids without considering the pore pressure. These cannot effectively describe the real behaviours of soil and hydraulic

conditions in surface erosion at the macroscale. Accordingly, equations for multi-phase mixtures at the macroscale are introduced in this section.

4.2.1 Equations for Fluids as Two-Phase Flow

A continuum-based approach established on the theory of multiphase flows is usually adopted to depict the behaviours of the particle–fluid mixture (e.g., [52, 74–85]). Among them, Aderson and Jackosn [74] adopted a volume-averaging technique to describe a system of particles and fluids in an average sense (see Fig. 9). By the volume-averaging technique, they used conversation equations to capture the behaviours of eroded particles and fluid phases within the fluid system by treating the solid phase as a fluid-like phase. Accordingly, this approach is called the two-fluid or two-phase flow model in the existing literature.

Following the work by Aderson and Jackson [74], Vardoulakis et al. [86] employed continuum-based mathematical models depicting sand production (i.e., sand particles are carried along with the produced oils in petroleum engineering) involving three phases: solid, liquid, and a fluidised solid phase representing eroded sands; Ouriemi et al. [87] earlier adopted a two-phase flow model modified by some closures to depict sheet flow (i.e., the flow of water with high bed shear stress over a uniform layer, resembling a sheet) in sediment transport of river hydraulic. Recent years have witnessed wide applications of numerous two-phase flow models for debris flow (e.g., [83, 84, 88, 89]). In this section, the fundamental conservation equations controlling the particle–fluid mixture [74] will be discussed.

In conservation equations describing the transport of particles in flow, two phases are considered: the solid phase and the fluid phase. The space occupied by the solid phase is expressed by a volume fraction ϕ, while that of the fluid phase is 1-ϕ. Both solid and fluid phases are controlled by the mass and momentum equations in an average sense, and their coupling is achieved by particle–fluid interaction terms. The mass conservation equations are given as follows:

$$\frac{\partial \phi \rho_s}{\partial t} + \frac{\partial \phi u_i^s}{\partial x_i} = 0 \tag{13}$$

$$\frac{\partial (1-\phi) \rho_f}{\partial t} + \frac{\partial (1-\phi) u_i^f}{\partial x_i} = 0 \tag{14}$$

where s and f denote solid and fluid, respectively; u_i^s and u_i^f denote the particle and fluid phase mean velocity, respectively.

Moreover, momentum conservation equations for fluid and solid phases are:

$$\rho_s \phi \left[\frac{\partial u_i^s}{\partial t} + u_i^s \frac{\partial u_i^s}{\partial x_j} \right] = \phi \frac{\partial \sigma_{ij}^s}{\partial x_j} + \phi \rho_s g_i + f_i \tag{15}$$

$$\rho_f (1-\phi) \left[\frac{\partial u_i^f}{\partial t} + u_i^f \frac{\partial u_i^f}{\partial x_j} \right] = (1-\phi) \frac{\partial \sigma_{ij}^f}{\partial x_j} + (1-\phi) \rho_f g_i - f_i \tag{16}$$

where ρ^s and ρ^f represent the particle and fluid phase density, respectively; σ_{ij}^s, σ_{ij}^f, and f_i are closure terms in above equations. σ_{ij}^s and σ_{ij}^f denote the particle and fluid stress tensors, respectively, which have the isotropic part and deviatoric parts as shown below:

$$\sigma_{ij}^s = -p^s \delta_{ij} + \tau_{ij}^s \tag{17}$$

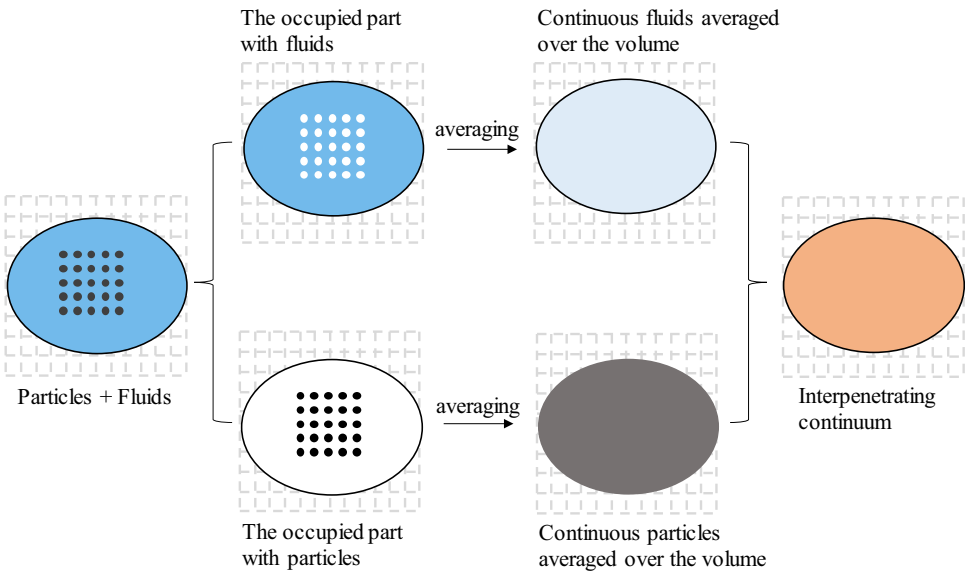

Fig. 9 Illustration of the volume-averaging technique (following [52])

$$\sigma_{ij}^{f} = -p^{f}\delta_{ij} + \tau_{ij}^{f} \tag{18}$$

where p^s and τ_{ij}^{s} are the isotropic stress and deviatoric stress of the particle fluid, respectively; p^f and τ_{ij}^{f} denote the isotropic stress and deviatoric stress of the fluid, respectively. These four terms are effectively expressed by the related constitutive model (i.e., the relation between stress and strain rate for the fluid) (e.g., [87, 90, 91]).

f_i is the particle–fluid interaction force in the averaging volume, related to the particle–fluid interaction force F_f in Eq. (1) at the particle scale. Existing studies (e.g., [75, 87, 91–94]) usually calculate f_i by considering the pressure gradient force $\nabla \cdot \left(p^f\right)$ and drag force f_{drag}:

$$f_i = \phi\nabla \cdot \left(p^f\right) + f_{drag} \tag{19}$$

$$f_{drag} = \phi(1-\phi)K(u_i^f - u_i^s) - \frac{1}{S_c}(1-\phi)Kv_t^f\frac{\partial\phi}{\partial x_i} \tag{20}$$

where v_t^f is the turbulent viscosity; S_c is the Schmidt number, and K is the drag parameter:

$$K = 0.75C_d\frac{\rho^s}{d} \parallel u^f - u^s \parallel (1-\phi)^{-h_{\mathrm{Exp}}}. \tag{21}$$

where C_d is the drag coefficient, expressed by an empirical equation as follows:

$$C_d = \begin{cases} \frac{24}{Re_p}(1 + 0.15Re_p^{0.687}), & Re_p \le 1000 \\ 0.44, & Re_p > 1000 \end{cases} \tag{22}$$

where the particulate Reynolds number Re_p is defied as:$Re_p = (1-\varnothing)\left|\left|u^f - u^f\right|\right|d/\nu^f$(in which ν^{f} represents the fluid kinematic viscosity).

4.2.2 Equations for Soils as Saturated Porous Media

Soils in the ocean can be regarded as saturated porous media, a two-phase mixture consisting of the solid skeleton and pore fluid. Biot [95] first proposed governing equations for saturated porous media, which have been widely adopted in numerous studies to investigate soil behaviours. Equations proposed by Biot [95] can be entirely established on the volume averaging idea in the two-phase flow. The derivation process is based on the principle of effective stress, constitutive model, and conservation equations of mass and momentum, with the last being derived directly from equations for two-phase flow.

The conservative equations for saturated porous media can be derived from equations for two-phase flow. The differences between them are: (i) The Eulerian description should be transformed into the Lagrangian description. (ii) The particle stress σ_{ij}^{s} should consider the effective stress principle. (iii) The particle–fluid interaction force only considers Darcy's law. Although most studies do not distinguish these points, we think these two sets of equations are different herein.

Accordingly, replacing the volume fraction ϕ in the Eqs. (13, 14) as $1-n$ (where n is the porosity) obtains the mass conservation equations for saturated porous media:

$$(1-n)\frac{\partial\rho_s}{\partial_t} + (1-n)\frac{\partial\rho_s u_i^s}{\partial x_i} = 0 \tag{23}$$

$$n\frac{\partial\rho_f}{\partial_t} + n\frac{\partial\rho_f u_i^f}{\partial x_i} = 0 \tag{24}$$

Equations (15, 16) by taking: (i): The convective terms $u_i^s\left(\partial u_i^s \big/ \partial x_j\right), u_i^f\left(\partial u_i^f \big/ \partial x_j\right)$ in Eq. (15, 16) are ignored in the saturated porous soils. (ii): The solid stress σ_{ij}^{s} is expressed as $\phi\sigma_{ij}^{s} = (1-n)\sigma_{ij}^{s} = \sigma_{ij}^{s'} - (1-n)p_w\delta_{ij}$ (where $\sigma_{ij}^{s'}$ is the solid effective stress can be expressed an effective constitutive model) according to the principle of effective stress. (iii): The fluid stress tensors σ_{ij}^{f} is simplified into $-p_w$; (iv): The particle–fluid interaction force f_i is taken as the drag force which is expressed as $f_i = r_w i = r_w\left(n\left(u_i^f - u_i^s\right)\big/ k\right)$ (where k is the Permeability coefficient) according to the Darcy' law. We can obtain the momentum conservation equation for the saturated porous media:

$$\begin{aligned}(1-n)\rho_s\frac{\partial u_i^s}{\partial t} =& (1-n)\frac{\partial\left(\sigma_{ij}^{s'} - (1-n)p_w\delta_{ij}\right)}{\partial x_j} \\ &+ (1-n)\rho_s g_i + r_w\frac{n\left(u_i^f - u_i^s\right)}{k}\end{aligned} \tag{25}$$

$$\rho_f n\frac{\partial u_i^f}{\partial t} = -n\frac{\partial p_w}{\partial x_j} + n\rho_f g_i - r_w\frac{n\left(u_i^f - u_i^s\right)}{k} \tag{26}$$

An isotropic ideal elastic constitutive model considering the compressibility of the solid by the pore pressure is adopted, which is expressed as $\sigma_{ij}^{s'} = 2\mu\varepsilon_{ij} + \lambda\delta_{ij}\varepsilon_{kk} + (1-\alpha)\delta_{ij}p_w$ (where $\alpha = 1 - K_T\big/K_S$ is the Boit parameter, K_T and K_S are the bulk modulus of solid skeleton and solid particle, respectively; $K_T = \lambda - 2\mu_s\big/3\lambda$ and μ_s are the Lame parameters in elastic theory).

Combining Eq. (23) with Eq. (24), the mass conservation equation for the mixture is expressed as:

$$\frac{\dot{p}_w}{M} + (\alpha - n)\frac{\partial u_i^s}{\partial x_i} + n\frac{\partial u_i^f}{\partial x_i} = 0 \tag{27}$$

where $1/M = \alpha - n/K_s + n/K_w$, K_w is the bulk modulus of water.

Combining Eq. (25) with Eq. (26), the momentum conservation equation for the mixture is expressed as:

$$\rho_f n\frac{\partial u_i^f}{\partial t} + (1-n)\rho_s\frac{\partial u_i^s}{\partial t} = \rho g_i + \frac{\partial \sigma_{ij}}{\partial x_j} \tag{28}$$

where σ_{ij} is the total stress for the mixture expressed as $\sigma_{ij} = (1-n)\sigma_{ij}^s + n\sigma_{ij}^f$.

The above basic equation for the saturated porous media can be expressed by three types: (1) the u–p formulation; (2) the u–U formulation; (3) the u–U-p formulation (where the velocity of the solid u_i^s is replaced as u; the velocity of a fluid u_i^f as U; the hydraulic pressure p_w as p).

5 Empiricism-Based Mathematical Model

The conservation equation is a comparatively theoretical approach to depicting soils and fluids. Another approach, usually in the form of empirical equations (referred to as the sediment transport model), can also serve as an alternating to depict different stages (i.e., the initiation and transport stage) of surface erosion. In this section, we will discuss these equations for the initiation and transport stages based on the foundational understanding established in Sect. 2.

5.1 Initiation Stage

Investigations via the experimental test, field test, and theoretical analysis have been conducted to determine the criterion of the initiation stage (e.g., [6, 96–102]). Most studies (e.g., [6, 97–100, 102]) have associated the criterion with the critical shear stress (i.e., Shields number), first proposed by Shields [50], or critical shear velocity, initially introduced by White [103]. Among them, the Shields number under sliding failure describing the initiation of particle movement is the most popular.

The initiation of surface erosion is related to the momentum conservation for the soil particle (i.e., Eq. (1)). Figure 10 depicts the forces controlling the initiation of particle movement. The drag force F_D and submerged weight F_G are considered. The additional mass force and Basset force are ignored because the particle is static before the initiation. The Saffman lift force and Magnus lift force are considered by an overall lift force F_L, which can be accessed via a widely used semi-empirical mathematical equation in sediment transport study [98, 99, 104]:

$$F_L = C_L A_P \frac{\rho_w u_b^2}{2} = \frac{\pi}{8} C_L \rho_w d^2 u_b^2 \tag{29}$$

in which C_L is the dimensionless coefficient of the lift force, with empirical expressions based on Reynolds number [104].

The resistant force F_R can be calculated by Coulomb's friction law [97, 102], expressed as follows:

$$F_R = \mu_s F_N = \mu_s \left(F_G - F_L \right) \tag{30}$$

in which μ_s is the friction coefficient, and F_N is the supporting force.

The force equilibrium controlling the sliding failure is given as $F_R = F_D$, where we substitute Eq. (29) and Eq. (30) into it to get the shear velocity u_b. By further utilising $\tau = \rho_w u_b^2$, we obtain the critical shear stress τ_{cr}. Using the normalized equation Eq. (31) (i.e., τ_{cr} is normalized by the submerged weight of the particle) results in the critical Shields number θ_{cr}.

$$\theta = \frac{\tau}{\rho_w g(G_s - 1)d} \tag{31}$$

Based on the idea of critical shear stress, many studies have employed the critical shear stress, critical flow velocity, and Shields number to describe the initiation stage via the experimental test, field test, and theoretical analysis. Table 2 summarises the empirical formulae of

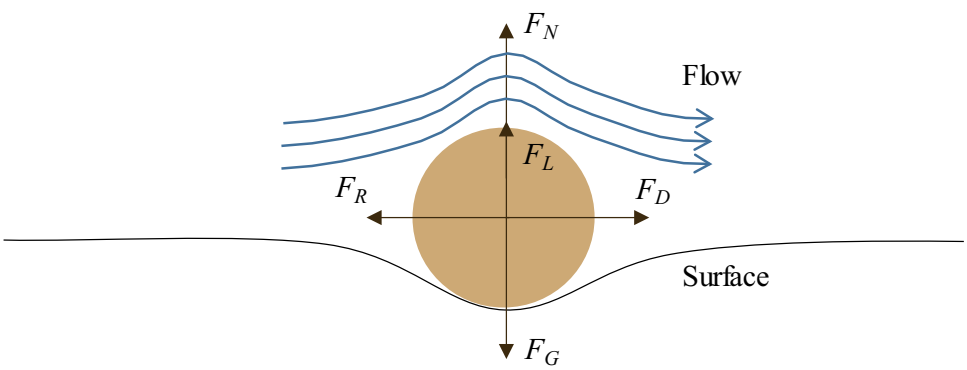

Fig. 10 Forces on a single particle on the horizontal mudline during the initiation stage

Table 2 Summary of equations for the critical stress or the Shields number

Equation	Notes:	References
$\tau_{cr0} = 0.63d_{50}$	d_{50}: the median diameter of soils	Shields [50]
$\theta_{cr0} = \begin{cases} 0.24d_*^{-1}, 1 < d_* \le 4 \\ 0.14Dd_*^{-0.64}, 4 < d_* \le 10 \\ 0.04d_*^{-0.1}, 10 < d_* \le 20 \\ 0.013d_*^{-0.29}, 20 < d_* \le 150 \\ 0.055, 150 < d_* \end{cases}$	d_*: the dimensionless grain size parameter, followed as $d_* = d\left[g(G_s-1)g/\nu^2\right]^{1/3}$(where ν is the fluid viscosity coefficient)	Rijn [198]
$\tau_{cr} = \frac{2(G_s-1)dc_1 f}{c_2}\frac{(\tan\varphi\cos\alpha_s - \sin\alpha_s)}{C_D + C_L\tan\varphi}$	α_s: the slope angle φ: the angle of repose of the soils c_1 and c_2: the correction factors for volume and area of particles f: the friction coefficient	Chiew and Parker [109]
$\tau_{cr0} = -0.015(\rho_s - 1000)^{0.73}$	ρ_s: the density of soils	Mitchener and Torfs [199]
$\theta_{cr} = \theta_{cr0}\left(\cos\beta_s\sqrt{1 - \frac{\sin^2\alpha_s\tan^2\beta_s}{\mu_s^2}} - \frac{\cos\alpha_s\sin\beta_s}{\mu_s}\right)$ $\theta_{cr0} = 0.3/\left(1 + 1.2d_*\right) + 0.055\left[1 - e^{-0.02d_*}\right]$	α_s: the bed slope angle, β_s: the angle between the flow and downslope direction of the bed μ_s: the friction coefficient	Soulsby [107]
$\theta_{cr0i} = \frac{0.1}{\left[\log\left(19d_i/d_{s0}\right)\right]^2}$	d_i: the size of i particle θ_{cr0}: the critical dimensionless shear stress for particle size of d_i	Egiazaroff [105]
$\theta_{cr0i} = \begin{cases} \theta_{ca}\frac{d_i}{d_a}, \frac{d_i}{d_a} < 1.0 \\ \theta_{ca}(\frac{\log 8}{\log(8d_i/d_a)})^2, \frac{d_i}{d_a} > 1.0 \end{cases}$	d_a: the average particle size of the mixture and θ_{ca}: the critical dimensionless shear stress for particle size of d_a	Hayashi et al. [106]
$v_{cr0} = \begin{cases} 2.33d_*^{-0.25}(R/d_{50})^{1/6}(\rho' g d_{50})^{1/2}, d_* \le 10 \\ 1.08d_*^{1/12}(R/d_{50})^{1/6}(\rho' g d_{50})^{1/2}, 10 < d_* \le 150 \\ 1.65(R/d_{50})^{1/6}(\rho' g d_{50})^{1/2}, 150 < d_* \end{cases}$	R: the hydraulic radius	Hager and Oliveto [200]
$\tau_{cr0} = \frac{2}{3}\gamma_w d(G_s - 1)\tan\varphi$	φ: the angle of repose of the soils	Annandale [201]
$\tau_{cr0} = 6.8(PI)^{1.68}P^{-1.73}e^{-0.97}$	PI: plasticity index (%) e: Porosity ratio of soils	Chang and Zhang [202]

critical shear stress. The empirical expression for critical Shields number θ_{cr} for the initiation stage was originally obtained based on a horizontal mudline (i.e., θ_{cr0}). Detailed empirical equations for critical Shields number θ_{cr0} can be found in the works of Egiazaroff [105], Hayashi et al. [106], Soulsby [107], and Wu et al. [108]. The derivation was later extended to include inclined the mudline (e.g., [107, 109]). Among them, the most prevalent one is proposed by Soulsby [107].

While empirical equations linking to the Shields number are effective in quantifying the initiation stage of surface erosion in practical scenarios, their applications require considerations of several factors: (i) initiation modes: different modes (e.g., sliding, uplifting, and rolling) need different empirical equations for description [97, 102]. (ii) particle characteristics: the variation of the particle's size or shape can influence the initiation [96] (iii) hydraulic conditions: the influence of flow condition (e.g., the water depth, water velocity, and the local turbulence) on the critical shear stress should be considered [110].

5.2 Transport Stage

Once particles start moving, they enter the complex transport process discussed in Subsection. 2.2. Different sets of equations specifically oriented for bed-load transport and suspended-load transport particles can be used to describe the behaviours of particles during transport. It is worth noting that the equations for bed-load and suspended-load transport in the work are suitable for conditions without waves. When considering wave conditions, these formulas should be adapted accordingly. For a detailed description of the transport stage under wave conditions, refer to Sumer [60].

5.2.1 Equations for Bed-Load Transport

The bed-load transport rate q_b, representing the volume of sediment transported per second per unit channel width, is widely employed to quantify the bed-load transport. Various methods can be utilised to determine the value of q_b: (i) Deterministic models: the deterministic models typically incorporate space-average expressions. Table 3 lists the deterministic models for the bed-load transport rate q_b. Note that the value of q_b is expressed via a scaled factor $\left[\left(\rho_s/\rho_f-1\right)gd_*^3\right]^{0.5}$ (i.e., Eq. (32)) in these models. Among these models, Meyer-Peter and Müller's empirical formula is the popular choice. (ii) Probabilistic model: probabilistic models emphasise the inherent uncertainty in sediment transport. The challenge of implementing such a model into numerical simulations lies in accurately estimating the uncertainties [51].

$$q_{b\_\mathrm{scaled}}=\frac{q_b}{\left[\left(\frac{\rho_s}{\rho_f}-1\right)gd_*^3\right]^{0.5}} \tag{32}$$

5.2.2 Equations for Suspended-Load Transport

Suspended-load transport is relatively more complicated. To simplify the complexities, the particle streamline velocity is mostly simply assumed to be the same as the fluid velocity. Additionally, many studies [6, 18, 51] depict the suspended-load transport as diffusion and convection of sediment concentration with a boundary value c_a (see in Fig. 11), which is given as follows:

$$\frac{\partial c}{\partial t}+(\mathbf{u}+\mathbf{w}_s)\nabla c=\nabla[(\nu+\nu_s)\nabla c] \tag{33}$$

where c denotes the volume concentration of the suspended-load transport particles, ν_s is the diffusion coefficient of the

Table 3 Summary of equations for bed-load transport rate

Equation for q_{b_scaled}	Notes	References
$\mathrm{e}^{0.391(1/\theta)}\frac{\sqrt{\frac{2}{3}+\frac{36\eta^2}{gd^3\rho_f\Delta\rho}}-\sqrt{\frac{36\eta^2}{gd^3\rho_f\Delta\rho}}}{0.465}$	η: the viscosity of the fluid	Einstein [203]
$C_b(\theta-\theta_{cr})^{1.5}$	C_b: the bed-load transport coefficient	Meyer-Peter and Müller [204]
$\frac{1-\frac{1}{\sqrt{\pi}}\int_{-0.156f\frac{1}{\theta}-2}^{0.156f\frac{1}{\theta}-2}\mathrm{e}^{-t^2}\mathrm{d}t}{27f_c\left(2-\frac{1}{\sqrt{\pi}}\int_{-0.156f\frac{1}{\theta}-2}^{0.156f\frac{1}{\theta}-2}\mathrm{e}^{-t^2}\mathrm{d}t\right)}$	f: the correction function obtained experimentally for grain size dispersion f_c: the percentage of grains of a given size put into motion	Einstein [205]
$8.5\sqrt{2\tan\alpha/(3\psi)}(\theta-\theta_{cr})\theta^{0.5}$	$\tan\alpha$: the friction coefficient ψ: the drag coefficient	Bagnold [206]
$1-\frac{\log\left(1+2.45(\frac{\rho_f}{\rho_s})^{0.4}\theta_{cr}^{0.5}(\frac{\theta}{\theta_{cr}}-1)\right)}{2.45\left(\frac{\rho_f}{\rho_s}\right)^{0.4}\theta_{cr}^{0.5}\left(\frac{\theta}{\theta_{cr}}-1\right)}$	–	Yalin [207]
$4.93(\theta-\theta_{cr})^{1.60}$	–	Wong and Parker [208]

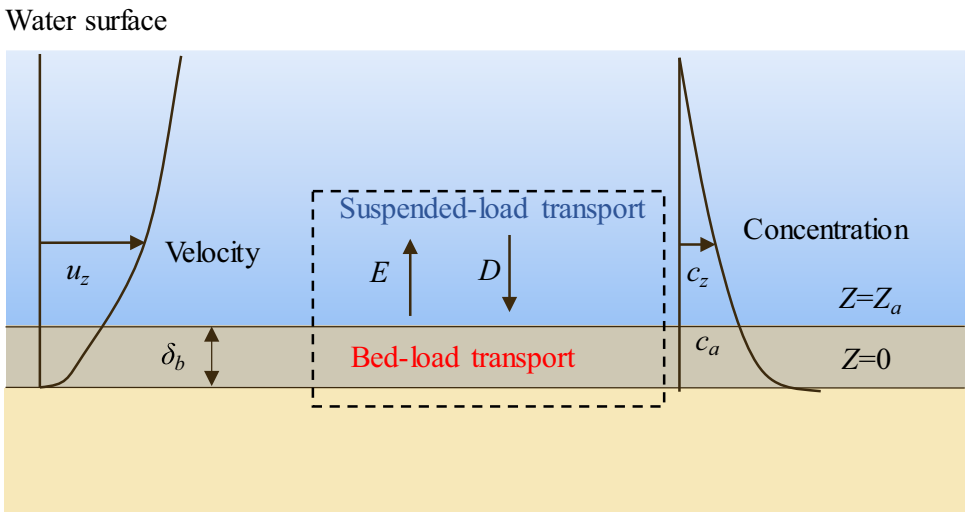

Fig. 11 Suspended-load transport particles experience entrainment and deposition

sediment, $\boldsymbol{u}$ is the velocity vector of the particle, $\boldsymbol{w_s}$ is the falling velocity vector, which has one scalar part w_s, can be linked to the particle size by empirical formulae (e.g., [107, 111–114]). In this context, the equation proposed by Soulsby [107] is presented:

$$w_s = \frac{\nu}{d_s}\left[\left(10.36^2 + 1.049 d_*^3\right)^{1/2} - 10.36\right] \tag{34}$$

For evaluating c_a, Zyserman and Fredsøe [115] suggested that:

$$c_a = \frac{0.331(\theta - 0.045)^{1.75}}{1 + 0.720(\theta - 0.045)^{1.75}} \tag{35}$$

As is mentioned in subection.2.2, the transition between bed-load transport and suspended-load transport is influenced by the fluid conditions, typically determined by the entrainment rate (E) and deposition rate (D). The entrainment rate (E) represents the rate at which sedimented particles are converted to suspension, while the deposition rate (D) describes the rate at which suspended particles settle back onto the mudline. Many studies related them to the Shields number [108, 116, 117]. For instance, Mastbergen and Van Den Berg [116] proposed an empirical equation relating the entrainment rate to the Shields number:

$$E = k_e(\theta - \theta_{cr})^n \tag{36}$$

where k_e is the entrainment coefficient; and n is the model parameter.

The deposition rate can be calculated by an empirical equation linked to the falling velocity w_s and near-bed suspended sediment concentration c_a.

$$D = c_a w_s \tag{37}$$

6 Continuum Mechanics-Based Numerical Modelling

In the earlier discussion, surface erosion can be seen as a boundary value problem governed by differential equations. This perspective allows for the application of continuum mechanics-based modelling approaches, which involve three key considerations: (i) Fluid domain: accurately modelling significant deformations in the fluid domain, delineating the fluid's free surface, and clarifying soil-fluid interactions crucial for surface erosion; (ii) Soil domain: focusing on soil mechanics, including fluid forces, and granular interactions; and (iii) Erosion processes: emphasizing macroscopic modelling of erosion behaviour, particularly the transport and initiation processes at the scale of small soil particles.

During the development of surface erosion simulations, two philosophies are employed depending on the above considerations (Table 4). The one-phase model focuses solely on the fluid domain, treating it as a single-phase flow while ignoring the soil domain. This approach simplifies the simulation by excluding equations related to soils. On the other hand, the Two-phase model considers both the fluid and

Table 4 Different continuum mechanics-based approaches capable of surface erosion simulation

Model	Movement description	Capable approaches	Used in surface erosion	References
One-phase-model (Only simulating the fluid phase)	Eulerian	FVM	√	Nagel et al. [93]
		FDM	√	Fan et al. [130]
		FEM	×	×
	Lagrangian	PFEM, MPM, SPH	×	×
	Eulerian–Lagrangian	ALE-FEM	√	[48],
Two-phase-model (Simulating both the fluid and solid phases)	Eulerian-Eulerian	FVM	√	Mathieu et al. [91]
		FDM	√	Ouriemi et al. [87],
		FEM	×	×
	Lagrangian-Lagrangian	PFEM	√	[150]
		MPM	√	[166]
		SPH	√	[73]
	Eulerian–Lagrangian	CEL	√	Lee et al. [187]
		FVM/FEM + MPM	√	Baumgarten et al. [180]
		FDM + MPM	×	×
		FVM/FDM/FEM + PFEM	×	×
		FVM/FDM/FEM + SPH	×	×

solid phases in the simulation of surface erosion, providing a more comprehensive representation.

In numerical simulation based on the two models, Lagrangian and Eulerian descriptions are widely used. The Lagrangian description associates the material movement with mesh nodes, being able to track free surfaces and interfaces between materials. However, it has shortcomings, such as mesh distortion in case of large deformation problems and the inability to capture the geometric change of the model due to the large deformation. Conversely, the Eulerian description views the materials as continuums on a spatially fixed grid, solving temporal changes of variables within the cells of this fixed grid. While this approach offers numerical stability in fluid dynamics simulation, it encounters challenges in precisely capturing the changing fluid–structure interfaces and fluid-soil interfaces.

Based on two tracking approaches of fluid and solid phases, the one-phase model is categorized into Eulerian, Lagrangian, and Eulerian–Lagrangian types, and the two-phase model into Eulerian-Eulerian, Lagrangian-Lagrangian, and Eulerian–Lagrangian types (Table 4). Different numerical frameworks in the Eulerian or Lagrangian description (e.g., FVM, FDM, FEM, PFEM, CEL, SPH, MPM) can be used to address the equations and simulate the process of surface erosion. Figure 12 depicts the proportion of seven continuum mechanics-based modelling approaches adopted in surface erosion according to the literature investigation results, it can be seen that the FVM, FDM, and ALE-FEM are frequently used in surface erosion simulation. The following section will discuss the detailed numerical schemes for surface erosion.

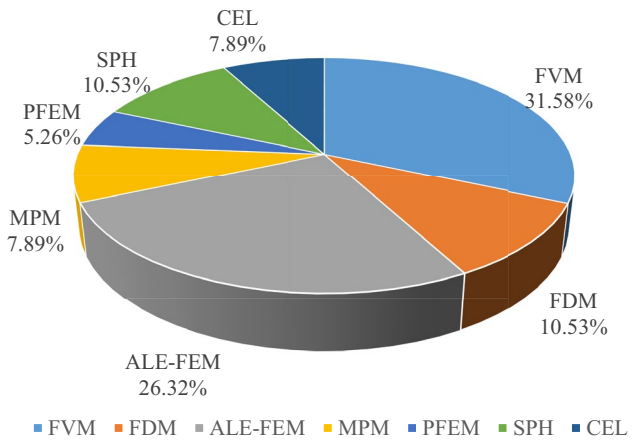

Fig. 12 Proportion of continuum mechanics-based approaches modelling surface erosion in the existing literature

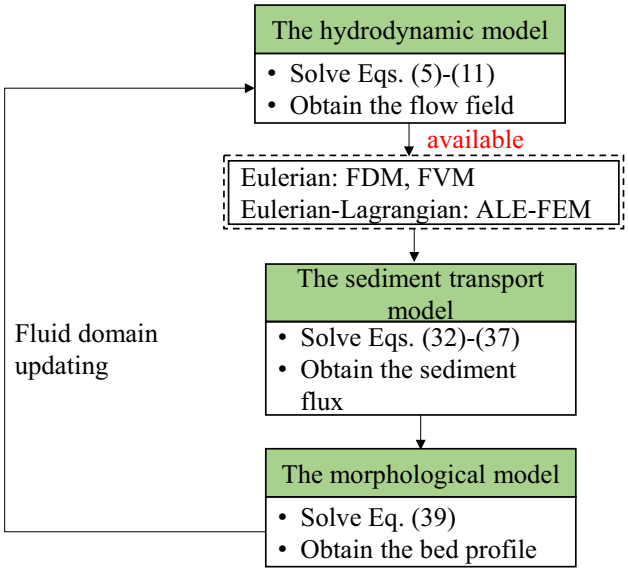

Fig. 13 The flow chart in one-phase model for surface erosion simulation

6.1 One-Phase Model

6.1.1 The Hydrodynamic Model

Most numerical simulations for surface erosion in the existing literature adopted the one-phase model, which only simulates the fluid phase and ignores the soil domain. Hence, it is also called one-phase flow model. Figure 13 depicts the flow chart of the one-phase flow model. The one-phase flow model requires a hydrodynamic model, sediment transport model and morphological model to simulate the fluid and the mudline geometry. The hydrodynamic model is used to simulate the fluid domain, usually achieved by using RANS equations along with the turbulence closures (i.e., Eqs. (5, 6, 7, 8, 9, 10, 11)). Based on the results of the hydrodynamic model, the flow velocity near the riverbed can be obtained. Furthermore, the sediment flux of the bed-load transport q_b and suspended-load transport q_s can be calculated via empirical formulae depicting the transport stage of surface erosion (i.e., Eqs. (32, 33, 34, 35, 36, 37)), this process is also called scour model (e.g., [35] or sediment transport model (e.g., [44, 46, 47]). Subsequently, the morphological model is employed to calculate the bed elevation based on the result of the sediment transport model. The morphological model achieves the evolution of mudline geometry, meanwhile, the fluid domain should also be updated based on the morphological model.

The key to the one-phase flow model is modelling the fluid domain, a key aspect of Computational Fluid Dynamics (CFD). In CFD, numerical methods based on the Eulerian approach, such as the finite volume method (FVM),

finite difference method (FDM), and finite element method (FEM), are widely used (refer to Table 4). On the other hand, Lagrangian-based numerical methods include Smoothed Particle Hydrodynamics (SPH), and the Arbitrary Lagrangian–Eulerian (ALE) concept can be also employed. However, according to existing literature, only FVM, FDM, and ALE-FEM have been utilized in modelling surface erosion.

Most simulations for the one-phase flow model are based on the Eulerian description and usually adopt finite volume and finite difference discretization techniques. Important contributions based on FVM are Olsen and Melaaen [118], Olsen and Kjellesvig [119], Roulund et al. [120], Liu and Garcia [121], Gothel [122], Khosronejad et al. [123], Baranya et al. [124], Stahlmann [125], Baykal et al. [126], Nagel et al. [93],Mei et al. [23], and Xu et al. [127]. Several finite volume-based fluid flow solvers have been employed such as OpenFOAM (e.g., [93, 126]), FOAMSCOUR (e.g., [121]), and EllipSys3D (e.g., [120]). One-phase model simulation using FDM can refer to Liang et al. [128], Burkow and Griebel [129], and Fan et al. [130]. The related fluid flow solvers are NaSt3D (e.g., [129]) and Flow3D (e.g., [130]). It is important to note that users can conveniently simulate surface erosion using the one-phase model based on the Eulerian description by using the current fluid flow solvers.

The ALE-FEM comes from FEM. The basic ideas of FEM involve discretizing the continuous space into a finite number of elements, approximating solutions within elements by interpolation functions, and translating differential equations into algebraic equations via methods such as the weighted residuals method. [131–134]. FEM with a Lagrangian description has been widely used for simulations in solid mechanics (e.g., [134–137]), while FEM with an Eulerian description is prevalent in problems such as fluid dynamics and heat transfer (e.g., [138–143]). For surface erosion, where the configuration change of the mudline (i.e., fluid-soil interface) should be updated in real-time, neither Lagrangian nor Eulerian form is optimal. Alternative approaches, such as those incorporating the Arbitrary Lagrangian–Eulerian scheme, may be more suitable. ALE combines the advantages of Lagrangian and Eulerian descriptions. It allows mesh nodes to move inside the model according to their velocities and avoid element distortion while updating model geometry via re-meshing, during which the field variables from the old mesh are mapped into the new one. Accordingly, FEM with Arbitrary Lagrangian–Eulerian description (i.e., ALE-FEM) can effectively handle the large deformation, free surface, and soil-fluid interactions in surface erosion simulation.

Surface erosion modelling using ALE-FEM can be found in existing studies (e.g., [33–35, 42–44, 46–49]). In the ALE-FEM scheme, the hydrodynamics model (i.e., the RANS equations with the turbulence equations Eqs. (5, 6, 7, 8, 9, 10, 11) usually needs to be solved by Petrov–Galerkin method (PG-FEM) [49, 144] rather than the conventional Galerkin method to avoid stress oscillations.

When modelling the hydrodynamics model based on the above approaches, it is essential to implement appropriate boundary conditions at the inlet boundary, outlet boundary, and free surface [47]. Additionally, a wall function sometimes needs to be used to estimate the flow velocity near the structure [43]:

$$u_1 = (u_f/\kappa)\ln(\Delta_1/z_0) \tag{38}$$

where u_1 is the tangential velocity for the first node near the wall; κ is the von Karman constant, which can be taken as 0.41; Δ_1 is the distance between the first nodal point and the wall and the wall; z_0 is the bed roughness length.

6.1.2 The Morphological Model

Based on results by the hydrodynamic model, the flow velocity near the riverbed can be obtained (i.e., Eq. (38)). Furthermore, the sediment flux of the bed-load transport q_b and suspended-load transport q_s can be calculated via the sediment transport model (in Sect. 5). Subsequently, the morphological model is simulated mainly by solving the bed level equation Eq. (39), based on the sediment flux of the bed-load transport q_b and suspended-load transport q_s:

$$\frac{\partial Z_b}{\partial t} = -\frac{1}{1-\lambda}\frac{\partial}{\partial x}\left(q_s + q_b\right) \tag{39}$$

where λ is the porosity of the sand, and Z_b is the bed elevation.

After solving the morphological model, two noteworthy issues arise. Firstly, the mudline slope calculated by the morphological model may be greater than the angle of repose of the soil, potentially leading to inaccuracies in simulation results. To mitigate this, a sand slide model can be employed [120, 130, 145]. Secondly, the nodes in the mesh will be updated according to the new mudline geometry (i.e., the node updating), the displacement of nodes can be obtained by the following equation [44]:

$$\nabla \cdot (\gamma \nabla S_i) = 0 \tag{40}$$

where S_i is the displacement field of the mesh points, S_1, S_2, *and* S_3 denote the displacement for x, y and z direction; and γ is a parameter that controls the mesh deformation.

Although the one-phase model can predict the final geometry of surface erosion, it is significant to note that this method ignores the temporal effect on sediment transport, i.e., the sediment transport capacity changes when the environment varies, such as boundary conditions; however, the change of sediment transport capacity may suffer a time lag [146]. As a result, the one-phase model simulation without

considering the time effect may be inaccurate in calculating the time evolution of surface erosion.

6.2 Two-Phase Model

The one-phase flow model can successfully model the fluid phase and the soil-fluid interface (i.e., erosion surface), but ignores the soils. By comparison, the two-phase model, which is capable of considering the behaviour of soils, seems to be more accurate for the modelling of surface erosion. This section will focus on the numerical approaches for the two-phase model.

6.2.1 Eulerian-Eulerian Type

The two-phase model tracking the soils and fluids using the pure Eulerian description is known as the Eulerian-Eulerian type. According to the literature review, this type normally solves equations for two-phase flow, effectively capturing the behaviours of both eroded particles and fluid phases within the fluid system. This is achieved by treating the solid phase as a fluid-like phase, following the Navier–Stokes framework (see Eqs. (13, 14, 15, 16, 17, 18, 19, 20, 21, 22) in subSect. 4.2.1). Consequently, the two-phase model in the Eulerian-Eulerian type is commonly referred to as the two-fluid or two-phase flow model [52]. Numerical approaches based on the Eulerian framework, such as FVM, FDM, and FEM, are available for the Eulerian-Eulerian model. However, in the context of surface erosion, FVM has been widely employed (see Table 4). Notable contributions to this field include the works of Amoudry et al. [92], Ouriemi et al. [87], Chauchat and Médale [75], Mathieu et al. [91], Nagel et al. [93], and Tofany and Wirahman [94].

A notable advantage of the two-fluid Eulerian-Eulerian model is its consideration of both the particle–fluid interaction and particle–particle interaction in surface erosion, distinguishing it from the one-phase flow model. Another advantage is that most two-fluid models can be widely simulated by numerical schemes, such as the finite volume method and finite difference method, which can employ commercial codes like FLUENT, OpenFOAM (e.g., [90, 91, 93]).

Despite these advantages, it's crucial to recognize the limitations in the current scope of two-phase flow models. First, the existing two-phase flow models do not account for the non-eroded soils, being unable to predict the reduction of the foundation's bearing capacities due to surface erosion. Besides, the simulation of two-phase flow models adopts the volume averaging technique (in subSect. 4.2.1). This technique is unable to be generalized to the broad range of concentrations of dispersed solids in a fluid [52]. Currently, most simulations using the continuum-based two-phase flow model are only suitable for sheet flow (i.e., amounts of particles move in a uniform layer for high flow velocity conditions) [18]. Meanwhile, the key to the two-phase flow model is the constitutive model of the solid phase, detailed constitutive models can refer to Lee et al. [90], Mathieu et al. [91], and Nagel et al. [93].

6.2.2 Lagrangian-Lagrangian Type

The two-phase model in the Eulerian-Eulerian framework mainly simulates fluid dynamics on a fixed grid. However, this approach falls short of accurately modelling the fluid-soil interface. In contrast, the pure Lagrangian framework excels in tracking both the fluid-soil interfaces. Within the Lagrangian framework, numerical approaches capable of addressing the large deformation problem include the Particle Finite Element Method (PFEM), Material Point Method (MPM), and Smoothed Particle Hydrodynamics (SPH). Among them, SPH is a mesh-free method. PFEM and MPM share the same idea of ALE. All these approaches have been employed in surface erosion simulations (see Table 4).

6.2.2.1 PFEM The particle finite element method (PFEM), an extension of the classical small strain finite-element method [147], was originally developed for the free-surface fluid flow problem [148] and fluid–structure interaction phenomena [149]. In the general procedure of PFEM, firstly, the continuum domain is represented as particles. Then, the mesh is generated by treating the particles as nodes. Note that this mesh usually adopts the Delaunay triangulation technique. After that, the governing equations for the continuum are solved and the positions of nodes are updated according to the solutions (e.g., velocities and displacements). If the movement of the particles significantly deforms the mesh, a new mesh is generated around the updated particle positions via the alpha shape method.

Existing surface erosion simulations using PFEM are comparatively rare. The existing simulations in the PFEM framework simulate the fluid domain by solving the equations for sing-phase flow in subSect. 4.1.1 and model the soil domain by solving equations for soils as solids in subSect. 4.1.2 (e.g., [150–152]).

As is shown in Fig. 14, a typical PFEM model for surface erosion involves three main components: the fluid part, the soil solid part, and the erosion interface. Firstly, the fluid part can be simulated by solving NS equations in the Lagrangian description. In parallel, the soil can be modelled by solving the momentum conservation equations (i.e., Eq. (12)). Then the erosion rule is employed to determine whether the interface is updated (i.e., the soil particles are transformed into the fluid particles), in specific, the soil element is removed

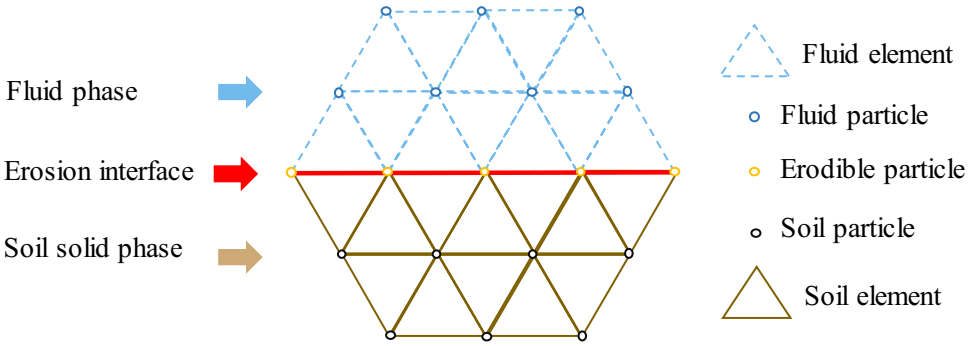

Fig. 14 Illustration of the fluid domain, soil domain, and the erosion surface in PFEM

from the solid surface, and a new fluid element will be generated in the same place.

The key factor of surface erosion simulation via PFEM is determining a rational erosion rule. Currently, Oñate et al. [153] adopted the critical frictional work to determine the initiation of erosion in PFEM. Galano et al. [150] utilized the Shields critical shear stress to obtain the entrainment rate. The integration of the entrainment rate over time and space gets soil mass loss. When the soil mass loss exceeds the original total mass of the soil particle, the interface will be updated [150].

6.2.2.2 MPM The material point method, also a continuum mechanics-based modelling method, solves the weak-form governing equations with the combination of the Eulerian (i.e., stationary grid) and Lagrangian (i.e., material points) descriptions. The Lagrangian material points are employed to document the material information (e.g., the velocity, displacement, stress, and strain), while the Eulerian gird is adopted to solve the governing equation. The grid will be discarded after the deformation to avoid mesh distortion. The information transforms between the Lagrangian particles and Eulerian grids via the shape function. [154].

Within the MPM framework, two primary approaches have been developed in the two-phase model: (i) The one-layer two-phase MPM uses a single set of material points to represent the two-phase media, as seen in works by Zhang et al. [155], Zabala and Alonso [156], Jassim et al. [157], Yerro et al. [158], and Ceccato et al. [159]. (ii) The two-layer two-phase MPM, on the other hand, uses two distinct sets of material points to separately discretize the solid and fluid phases, with examples including Abe et al. [160], Bandara and Soga [161], Liang et al. [162], and [54, 163, 164]. It is observed that the two-layer two-phase MPM approach has been predominantly used to model surface erosion, despite a limited number of studies employing the MPM framework in surface erosion simulations (e.g., [162, 163, 165–168]).

Figure 15 shows the two-layer two-phase MPM designed for simulating surface erosion such as overtopping,

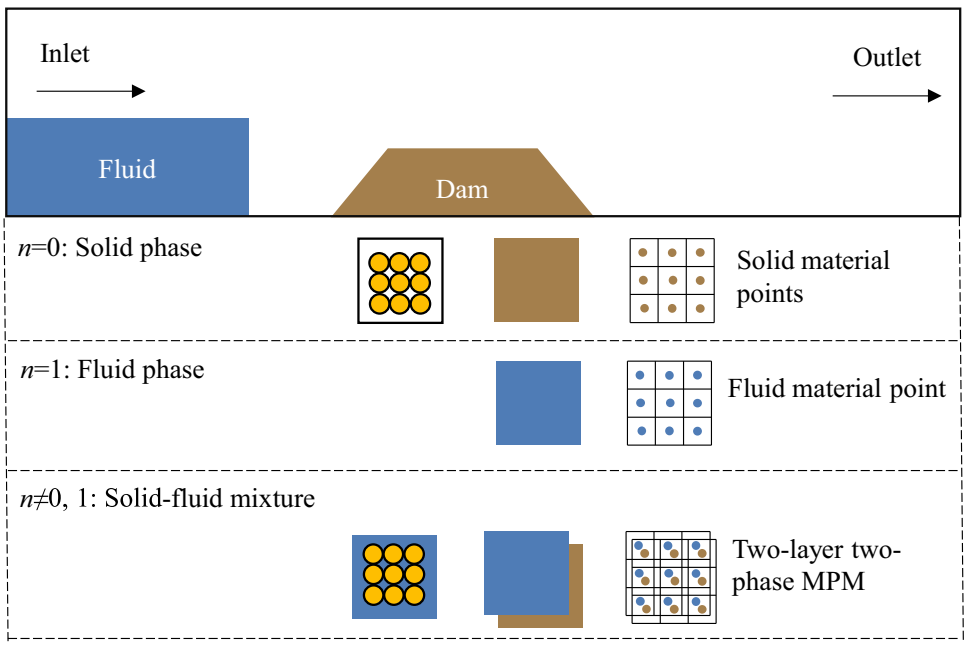

Fig. 15 Diagram of the two-layer two-phase MPM in overtopping simulations

employing conservation equations for both mass (i.e., Eq. (24) for fluid and Eq. (23) for solid) and momentum (i.e., Eq. (26) for fluid and Eq. (25) for solid) in saturated porous media (e.g., [163, 166, 167]). The method distinguishes solid and fluid phases with separate material points. Porosity n dictates the material state: $n=0$ for the pure solid, $n=1$ for the pure fluid, and intermediate values representing solid–fluid mixtures. The behaviour evolves from saturated soil ($0<n<n_{max}$) to fluid ($n>n_{max}$) as soil grains scatter and stresses decrease. Notably, the model simulates the erosion process by shifting from solid-like to fluid-like responses based on the porosity threshold, without directly calculating shear stress on solids.

6.2.2.3 SPH Smoothed Particle Hydrodynamics (SPH) is a mesh-free method that directly solves the strong-form governing equations using the Lagrangian description [169]. Initially developed for astrophysics applications, SPH has since been applied in fluid dynamics (e.g., [170, 171]) and geotechnical engineering (e.g., [164, 172–175]). In SPH, the continuum is represented by a set of particles, each carrying field information. The information of a particle can be determined by its neighbouring particles within a smoothing length h, using a smoothing function known as the kernel function W. The field information of a particle i and the spatial derivatives of the field function are computed as follows:

$$f(x_i) = \sum \frac{m_j}{\rho_j} f(\mathbf{x}_j) W_{ij}(r,h) \tag{41}$$

$$\nabla f(x_i) = \sum \frac{m_j}{\rho_j} f(x_j) \nabla_i W_{ij}(r,h) \tag{42}$$

where m_j and ρ_j are the mass and density of the neighbouring particle j respectively; $W_{ij}(r, h)$ is the kernel function, which is related to the smoothing length h and the distance r between particle i and j.

With the SPH idea, several studies have explored its application for simulating surface erosion [73, 176–178]. Notably, Zhou et al. [73] have successfully achieved the simulation of the entrainment, deposition, and re-entrainment processes in surface erosion. As illustrated in Fig. 16, a typical SPH model for surface erosion comprises three main components: the fluid part, the soil part, and the erosion model for the soil-fluid interface. The fluid continuum is modelled using the Navier–Stokes (NS) equations within the SPH framework, using the Herschel-Bulkley-Papanastasiou (HBP) model for fluid constitutive behaviour. Similarly, the soil part is represented as particles governed by the same NS equations. The erosion model simulates entrainment, deposition, and re-entrainment processes for soil particles using various constitutive models. Initially, un-eroded soil particles follow the Drucker-Prager (DP) model [179]. Upon meeting the erosion criterion, these particles are eroded and modelled according to the HBP fluid model, and when they satisfy the deposition criterion, they revert to the DP model. Overall, both original and deposited soil particles are assumed to follow the DP model, while water and eroded particles are represented by the HBP fluid model.

$$\frac{d\rho_i}{dt} = \rho_i \sum m_j \rho_j v_{ij} \bullet \nabla_i W_{ij}(r,h) \tag{43}$$

$$\frac{dv_i}{dt} = \sum m_j \left[\frac{\sigma_i + \sigma_j}{\rho_i \rho_j}\right] \nabla_i W_{ij}(r,h) + F_i \tag{44}$$

where v_{ij} is the difference between velocity v_i and v_j. σ is the total stress tensor, and F is an external force which is gravity in this study.

The fundamental concept of surface erosion simulation using the SPH model lies in transforming the constitutive models of the soils into fluid-like models based on the criteria for erosion, deposition, and re-erosion. These criteria are connected to equations that describe different stages of surface erosion (see Sect. 5). It is noteworthy that the SPH model shares similar transformation ideas of soil and particle behaviours with other numerical techniques such as the PFEM and MPM methods. Additionally, while its computational cost remains a challenge, some studies have

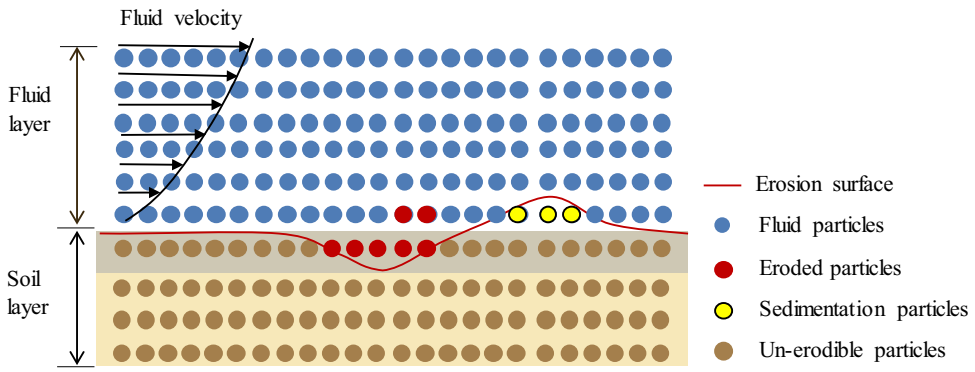

Fig. 16 Illustration of SPH in surface erosion simulation (from [73])

employed Graphics Processing Units (GPUs) to accelerate computation, effectively mitigating this issue [73, 176, 178].

6.2.3 Eulerian–Lagrangian Type

The two-phase model in the Eulerian–Lagrangian type is a hybrid approach for simulating surface erosion. In this model, the fluid domain is tracked using the Eulerian framework, while the solid domain employs the Lagrangian framework. This idea combines the robustness of the Eulerian framework for simulating pure fluids and the Lagrangian framework's effectiveness for simulating the granular phase of the mixture. Within the Eulerian–Lagrangian hybrid framework, various combinations are possible, as indicated in Table 4. However, existing studies typically adopt hybrid models such as CEL (i.e., Coupled Eulerian–Lagrangian), FVM-MPM, and FEM-MPM. Significant contributions in the field of surface erosion simulation based on FVM-MPM include the works of Baumgarten et al. [180] and Tran et al. [181]. For studies utilizing FEM-MPM, references include Wang and Wang et al. [182], Pan et al. [183], and Zhu et al. [184]. These hybrid models build upon the foundational models previously discussed. Research on the CEL technique is notably presented by Lee and Jeong [185], Jeong and Lee [186], and Lee et al. [187]. This subsection will specifically focus on the CEL technique.

The CEL model effectively addresses large deformation problems by integrating Eulerian and Lagrangian materials through Eulerian–Lagrangian contact, which can be employed by a commercial code Abaqus (e.g., [185–190]). In the CEL method, the Lagrangian structure is allowed to deform freely within the Eulerian mesh. The movement of Eulerian material is governed by the Eulerian volume fraction (EVF) of each element, which is defined as follows: when EVF = 1, the element is filled with Eulerian material,when EVF = 0, the element contains no material; and when $0 < \mathrm{EVF} < 1$, the element is partially filled with Eulerian material (see Fig. 17a). The interaction between Eulerian and Lagrangian domains typically employs a general contact approach based on the penalty contact method, where the velocity of the Lagrangian boundary can be converted into a force on the Eulerian region, while the pressures in the Eulerian material exert forces on the Lagrangian domain.

Several studies have utilized the CEL method to model debris flow (see [185–187]). Figure 17b illustrates the CEL model for debris flow simulation, where the bedrock is represented using Lagrangian elements, while the initial

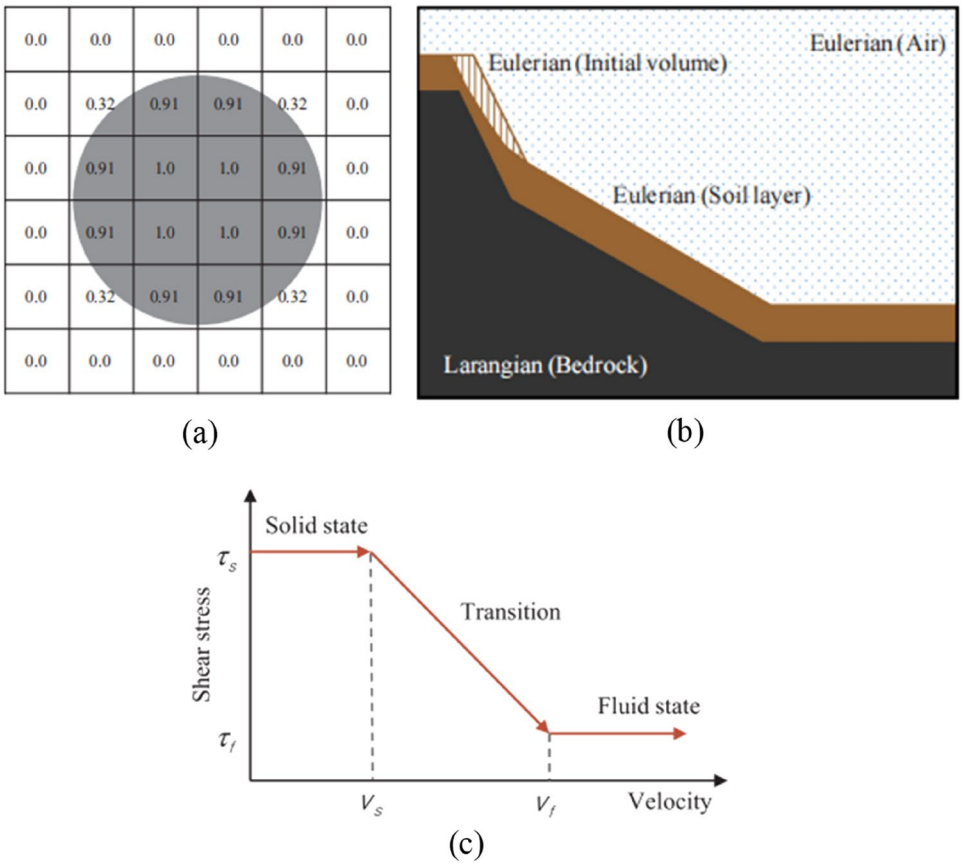

Fig. 17 Illustration of CEL method in debris flow simulation: (**a**) The scheme of Eulerian volume fraction (EVF) technique; (**b**) the debris flow modelling using CEL; (**c**) The variation of shear strength of soil with velocity (from [185])

debris flow volume and eroded soil layer are modelled using Eulerian elements. To account for the entrainment process (i.e., the erosion of soils by the initial debris flow), the elasto-plastic behaviour of the soil layer before entrainment is transformed into fluid-like behaviour after entrainment based on the shear strength of the soil. Figure 17c depicts this transformation: if the velocity of the soil layer is smaller than v_s, the soil layer exhibits elasto-plastic behaviour as characterized by the Mohr–Coulomb model. If the velocity of the soil layer is less than v_f, the state is intermediate between solid and fluid, and if it is greater than v_f, the state follows a rheological behaviour similar to flow.

7 Discussion and Future Work

7.1 Discussion

Continuum mechanics-based numerical approaches provide significant advantages in solving complex boundary value problems and delivering rational assessments for large-scale engineering challenges. The numerical methods for surface erosion are detailed in Table 5, including both one-phase and two-phase models, each featured in distinct philosophies:

The one-phase model, the most prevalent approach in current surface erosion numerical analysis, simulates the erosion process using RANS equations for the fluid and empirical formulae for the mudline geometry. It is highly efficient in surface erosion simulation. However, it employed the equations for fluids not disturbed by soil particles, which does not satisfy the actual physical mechanism. Additionally, using empirical formulae limits its applicability, as they may not suit conditions beyond their derivation background.

In contrast, the two-phase model offers a more comprehensive analysis by incorporating the soil domain. Within this model, the Eulerian-Eulerian two-phase flow model effectively considers particle–fluid and particle–particle interactions, facilitating commercial codes like FLUENT and OpenFOAM. Nevertheless, it is crucial to acknowledge that the Eulerian-Eulerian type primarily suits sheet flow conditions, characterised by a uniform particle layer moving under high flow velocity [18]. Moreover, considering particle–fluid interaction terms are limited to pressure gradient and drag forces, which might not fully encapsulate real-world conditions. The Lagrangian-Lagrangian type, such as PFEM, MPM, and SPH, excels in tracking fluid–solid interfaces and soil deformation. However, it predominantly focuses on the entrainment phase of erosion, neglecting deposition. This focus, coupled with a reliance on empirical erosion formulae, limits its accuracy in fully capturing surface erosion (e.g., [73, 150, 166]). Lastly, the Eulerian–Lagrangian hybrid type combines the Eulerian approach's fluid simulation strengths with the Lagrangian method's efficiency in representing soils. However, research on its application to surface erosion simulation remains scarce.

7.2 Future Work

Continuum mechanics-based numerical simulations have widely been employed in replicating the large-scale physical processes of surface erosion. Despite their achievements, there still exist some future works:

A rational numerical approach for modelling surface erosion without obstructing structures (e.g., riverbed erosion, overtopping) as a typical fluid-soil interaction problem still needs development. It is related to the following challenges: (i) The seabed: Existing studies often concentrate on the erosion surface while overlooking the underlying soils. Although the two-phase model has considered soils, the soils are limited in saturated sands. Additionally, although few constitutive models are used to illustrate the behaviours of soils (e.g., [73]), these constitutive models frequently neglect the influence of surface erosion conditions. (ii) The eroded particles: the initiation, transport, and sedimentation

Table 5 Comparisons between different finite element approaches in the existing literature

Model	Approaches	Advantages	limitations
The one-phase model	ALE-FEM, FVM, FDM	High efficiency	The boundedness of empirical formulae
The two-phase model	FVM (Eulerian-Eulerian)	Considering particle–fluid interaction and particle–particle interactions, Available of the commercial codes	Suitable for the sheet flow
	PFEM, MPM, SPH (Lagrangian-Lagrangian)	Tracking both the interface and the entire soil particles	Inaccuracies of the whole erosion-induced surface
	CEL, FVM-MPM, FEM-MPM (Eulerian-Lagrangian)	Combining the robustness of the Eulerian framework for simulating fluids and the Lagrangian framework's effectiveness for simulating the granular mixture	Few works on surface erosion simulation

of eroded particles in flow, which has the feature of particle scale, is difficult to simulate by continuum mechanics at the macroscale. (iii) The marine environment: The marine environment involves complex wave-current coupling, and while some simulations have addressed the wave-current coupling (e.g., [47, 145]), further improvements are needed to enhance the robustness and efficiency of these models. Additionally, two-phase models, such as PFEM and MPM, which account for wave-current coupling, remain underdeveloped.

More significant work is extending the simulations mentioned above to surface erosion with the disturbance of structures (e.g., local scour), a typical fluid–structure-soil interaction problem, which is more complex due to (i) Fluid–structure interaction: Various structures (e.g., monopiles, jacket foundations, and the mooring lines) are subjected to dynamic loading by the fluid. This interaction can influence the flow condition. (ii) Soil-structure interaction: the dynamically loading structures (e.g., the mooring line) will influence the surrounding soil characteristics, which can significantly influence the behaviour of surface erosion. Although many models consider the structures in simulation (e.g., [34, 48, 49, 191]), these models do not achieve fully coupled simulation involves the hydraulic condition (waves and currents), dynamically loaded structure, and soil conditions.

In summary, rational continuum mechanics-based modelling can accurately estimate the evolution of surface erosion in complex fluid-soil interaction problems and fluid–structure-soil interaction problems.

8 Conclusion

This study comprehensively reviewed the application of continuum mechanics-based modelling approaches in soil surface erosion and compared different numerical methods. First, the main physical processes and factors of surface erosion were summarised. After that, the mathematical equations of developing numerical simulations were reviewed from physics-based governing equations of soils and fluids and empiricism-based equations describing different stages of surface erosion. Finally, two existing models based on different numerical approaches were presented in terms of Eulerian and Lagrangian descriptions. The main conclusions are made as follows:

(1) Despite surface erosion being a multiphase phenomenon influenced by factors like soil, hydraulic, and structure conditions, numerous physics-based or empiricism-based mathematical models have been developed to characterise it.
(2) The one-phase model, widely employed using the FVM, FDM, and ALE, simulates the fluid phase using NS equations and the mudline geometry using empirical formulae. The accuracy is dependent on the empirical formulae.
(3) The two-phase model, which accounts for fluid and solid phases, provides a more detailed assessment of surface erosion. Approaches within the Lagrangian framework, such as PFEM, MPM, and SPH, are particularly effective at capturing fluid–solid interactions and soil deformations. Despite these strengths, these approaches do not completely simulate the entire physical processes, including the initiation and transport stages.
(4) A comprehensive and rational continuum mechanics-based modelling approach that accurately estimates the evolution of surface erosion within complex fluid-soil and fluid–structure-soil interaction scenarios remains a work in progress.

Acknowledgements This research is financially supported by the Research Grants Council (RGC) of Hong Kong Specia Administrative Region Government (HKSARG) of China (Grant No. 15226322, 15229223, 15232224), and the Research Centre for Nature-based Urban Infrastructure Solutions at The Hong Kong Polytechnic University.

Author Contributions Hang Feng wrote the main manuscript text and prepared all figures; Zhen-Yu Yin provided ideas, revised the manuscript and figures, provided finial support; Maozhu Peng provided technical help and did most of the revisions of the manuscript; Qimeng Guo helped to refine the manuscript text and figures; joined all discussions.

Funding Open access funding provided by The Hong Kong Polytechnic University. The research Grants Council (RGC) of Hong Kong Specia Administrative Region Government (HKSARG) of China (Grant No. 15226322, 15229223, 15232224).

Data Availability No datasets were generated or analysed during the current study.

Declarations

Competing Interests The authors declare no competing interests.

References

1. Wang X, Tang Y, Huang B, Hu T, Ling D (2021) Review on numerical simulation of the internal soil erosion mechanisms using the discrete element method. Water 13(2):169
2. Yang J, Yin ZY, Laouafa F, Hicher PY (2020) Hydromechanical modeling of granular soils considering internal erosion. Can Geotech J 57(2):157–172
3. Yang J, Yin ZY, Laouafa F, Hicher PY (2020) Three-dimensional hydromechanical modeling of internal erosion in dike-on-foundation. Int J Numer Anal Meth Geomech 44(8):1200–1218
4. Yang J, Yin ZY, Laouafa F, Hicher PY (2022) Numerical analysis of internal erosion impact on underground structures: application to tunnel leakage. Geomech Energy Environ 31:100378
5. Bonelli S (2012) Erosion of geomaterials
6. Zhang L, Peng M, Chang D, Xu Y (2016) Dam failure mechanisms and risk assessment
7. Clarkson L, Williams D (2021) An overview of conventional tailings dam geotechnical failure mechanisms. Mining Metall Explor 38(3):1305–1328
8. Li J, Guo Y, Lian J, Wang H (2023) Mechanisms, assessments, countermeasures, and prospects for offshore wind turbine foundation scour research. Ocean Eng 281:114893
9. Mercier F, Golay F, Bonelli S, Anselmet F, Borghi R, Philippe P (2014) 2D axisymmetrical numerical modelling of the erosion of a cohesive soil by a submerged turbulent impinging jet. Eur J Mech-B/Fluids 45:36–50
10. Sharif AR, Atkinson JF (2012) Model for surface erosion of cohesive soils. J Hydraul Eng 138(7):581–590
11. Dean RG, Galvin CJ Jr (1976) Beach erosion: causes, processes, and remedial measures. Crit Rev Environ Sci Technol 6(3):259–296
12. Guan DW, Xie YX, Yao ZS, Chiew YM, Zhang JS, Zheng JH (2022) Local scour at offshore windfarm monopile foundations: a review. Water Sci Eng 15(1):29–39
13. Majid SA, Tripathi S (2021) Pressure-flow scour due to vertical contraction: a review. J Hydraul Eng 147(12):03121002
14. Shahriar AR, Ortiz AC, Montoya BM, Gabr MA (2021) Bridge Pier Scour: an overview of factors affecting the phenomenon and comparative evaluation of selected models. Transp Geotech 28:100549
15. Tafarojnoruz A, Gaudio R, Dey S (2010) Flow-altering countermeasures against scour at bridge piers: a review. J Hydraul Res 48(4):441–452
16. Tang ZH, Melville B, Singhal N, Shamseldin A, Zheng JH, Guan DW, Cheng L (2022) Countermeasures for local scour at offshore wind turbine monopile foundations: a review. Water Sci Eng 15(1):15–28
17. Tripathi RP, Pandey KK (2022) Scour around spur dike in curved channel: a review. Acta Geophys 70(5):2469–2485
18. Zhao M (2022) A review on recent development of numerical modelling of local scour around hydraulic and marine structures. J Marine Sci Eng 10(8):1139
19. Benedict ST, Caldwell AW (2014) A pier-scour database: 2,427 field and laboratory measurements of pier scour (No. 845). US Geological Survey
20. DNVGL (2016) DNVGL-ST-0126 support structure for wind turbines. Det Norske Veritas, Oslo
21. Aman S, Rezk MA, Nasr R (2023) Effect of tailwater depth on non-cohesive earth dam failure due to overtopping. Ain Shams Eng J 14(8):102034
22. Foster M, Fell R, Spannagle M (2000) The statistics of embankment dam failures and accidents. Can Geotech J 37(5):1000–1024
23. Mei S, Chen S, Zhong Q, Shan Y (2022) Detailed numerical modeling for breach hydrograph and morphology evolution during landslide dam breaching. Landslides 19(12):2925–2949
24. Chiew YM (1990) Mechanics of local scour around submarine pipelines. J Hydraul Eng 116(4):515–529
25. Chiew YM (1992) Effect of spoilers on scour at submarine pipelines. J Hydraul Eng 118(9):1311–1317
26. Dey S, Singh NP (2008) Clear-water scour below underwater pipelines under steady flow. J Hydraul Eng 134(5):588–600
27. Mao Y (1987) The interaction between a pipeline and an erodible bed. Series Paper Technical University of Denmark, (39)
28. Penna N, Coscarella F, Gaudio R (2020) Turbulent flow field around horizontal cylinders with scour hole. Water 12(1):143
29. Sumer BM, Truelsen C, Sichmann T, Fredsøe J (2001) Onset of scour below pipelines and self-burial. Coast Eng 42(4):313–335
30. Wang C, Yuan Y, Liang F, Tao J (2022) Experimental investigation of local scour around cylindrical pile foundations in a double-layered sediment under current flow. Ocean Eng 251:111084
31. Wu Y, Chiew YM (2013) Mechanics of three-dimensional pipeline scour in unidirectional steady current. J Pipeline Syst Eng Pract 4(1):3–10
32. Yu P, Chen J, Zhou J, Li J, Yu L (2023) Experimental investigation of local scour around complex bridge pier of sea-crossing bridge under tidal currents. Ocean Eng 290:116374
33. Lu L, Li Y, Qin J (2005) Numerical simulation of the equilibrium profile of local scour around submarine pipelines based on renormalized group turbulence model. Ocean Eng 32(17–18):2007–2019
34. Peng D, Zhao L, Zhou C, Mao J (2023) Finite element numerical simulation of local scour of a three-dimensional cylinder under steady flow. Int J Comput Fluid Dynam 36(10):892–907
35. Zhao M, Cheng L (2010) Numerical investigation of local scour below a vibrating pipeline under steady currents. Coast Eng 57(4):397–406
36. Hu D, Tang W, Sun L, Li F, Ji X, Duan Z (2019) Numerical simulation of local scour around two pipelines in tandem using CFD–DEM method. Appl Ocean Res 93:101968
37. Ma H, Zhang S, Li B (2023) Numerical investigation of local scour around twin piles under steady current using CFD-DEM coupling method. Comput Geotech 164:105805
38. Schmeeckle MW (2014) Numerical simulation of turbulence and sediment transport of medium sand. J Geophys Res Earth Surf 119(6):1240–1262
39. Song S, Park S (2022) Unresolved CFD and DEM coupled simulations on scour around a subsea pipeline. J Marine Sci Eng 10(5):556
40. Yang J, Low YM, Lee CH, Chiew YM (2018) Numerical simulation of scour around a submarine pipeline using computational fluid dynamics and discrete element method. Appl Math Model 55:400–416
41. Zhang Y, Zhao MKCS, Kwok KC, Liu MM (2015) Computational fluid dynamics-discrete element method analysis of the onset of scour around subsea pipelines. Appl Math Model 39(23–24):7611–7619
42. Ajdehak E, Zhao M, Cheng L, Draper S (2018) Numerical investigation of local scour beneath a sagging subsea pipeline in steady currents. Coast Eng 136:106–118
43. Brørs B (1999) Numerical modeling of flow and scour at pipelines. J Hydraul Eng 125(5):511–523
44. Dhamelia V, Zhao M, Hu P (2023) Numerical investigation of local scour around a vertically vibrating subsea pipeline under steady flow. Ocean Eng 285:115437
45. Golay F, Lachouette D, Bonelli S, Seppecher P (2011) Numerical modelling of interfacial soil erosion with viscous incompressible flows. Comput Methods Appl Mech Eng 200(1–4):383–391

46. Liu MM (2021) Numerical investigation of local scour around submerged pipeline in shoaling conditions. Ocean Eng 234:109258
47. Liu MM, Lu L, Teng B, Zhao M, Tang GQ (2016) Numerical modeling of local scour and forces for submarine pipeline under surface waves. Coast Eng 116:275–288
48. Zhao L, Guo B, Bai X, Zhang W, Li T, Williams JJR (2016) Finite element modelling of local scour below a pipeline under steady currents. Int J Comput Fluid Dynamics 30(1):1–6
49. Zhao M, Cheng L, Teng B, Dong G (2007) Hydrodynamic forces on dual cylinders of different diameters in steady currents. J Fluids Struct 23(1):59–83
50. Shields A (1936) Anwendung der Aehnlichkeitsmechanik und der Turbulenzforschung auf die Geschiebebewegung. PhD Thesis Technical University Berlin
51. Zhang W (2015) Sediment Transport Models, Encyclopedia of Marine Geosciences
52. Ibrahim A, Meguid MA (2020) Coupled flow modelling in geotechnical and ground engineering: an overview. Int J Geosynth Ground Eng 6:1–25
53. Madadelahi M, Acosta-Soto LF, Hosseini S, Martinez-Chapa SO, Madou MJ (2020) Mathematical modeling and computational analysis of centrifugal microfluidic platforms: a review. Lab Chip 20(8):1318–1357
54. Zhao Z, Zhou L, Bai L, Wang B, Agarwal R (2023) Recent advances and perspectives of CFD–DEM simulation in fluidized bed. Arch Comput Methods Eng 31(2):871–918
55. Sun W, Yu Z (2023) A novel correlation of bubble aspect ratio through analysis of gas/shear-thinning liquid two-phase flow in a bubble column. Exp Thermal Fluid Sci 149:110996
56. Hofland B, Battjes JA, Booij R (2005) Measurement of fluctuating pressures on coarse bed material. J Hydraul Eng 131(9):770–781
57. Ali SZ, Dey S (2017) Origin of the scaling laws of sediment transport. Proc R Soc A 473(2197):20160785
58. Lin C, Bennett C, Han J, Parsons RL (2010) Scour effects on the response of laterally loaded piles considering stress history of sand. Comput Geotech 37(7–8):1008–1014
59. Liu J, Chen X, Zhu Z, Wang B (2019) Investigation of scour effect on tensile capacity of suction caissons considering stress history of sand. Mar Georesour Geotechnol 37(9):1044–1056
60. Sumer BM (2002) The mechanics of scour in the marine environment. World Scientific
61. Sumer BM, Christiansen N, Fredsoe J (1992) Time scale of scour around a vertical pile. In: ISOPE International Ocean and Polar Engineering Conference, ISOPE
62. Sumer BM, Christiansen N, Fredsøe J (1997) The horseshoe vortex and vortex shedding around a vertical wall-mounted cylinder exposed to waves. J Fluid Mech 332:41–70
63. Gao FP, Yang B, Wu YX, Yan SM (2006) Steady current induced seabed scour around a vibrating pipeline. Appl Ocean Res 28(5):291–298
64. Rui S, Zhou W, Shen K, Guo Z (2023) Review on seabed trenches induced by mooring lines and analyses of anchor bearing capacity. J Mar Sci Appl 22(2):296–310
65. Ahmad N, Kamath A, Bihs H (2020) 3D numerical modelling of scour around a jacket structure with dynamic free surface capturing. Ocean Eng 200:107104
66. Sajjan K, Shah NA, Ahammad NA, Raju CSK, Kumar MD, Weera W (2022) Nonlinear Boussinesq and Rosseland approximations on 3D flow in an interruption of Ternary nanoparticles with various shapes of densities and conductivity properties. AIMS Math 7(10):18416–18449
67. Wilcox DC (1998) Turbulence modeling for CFD. 2, pp 103-217
68. Alonso EE, Gens A, Josa A (1990) A constitutive model for partially saturated soils. Géotechnique 40(3):405–430
69. Kavvadas M, Amorosi A (2000) A constitutive model for structured soils. Géotechnique 50(3):263–273
70. Lade PV (2005) Overview of constitutive models for soils. In: Soil constitutive models: evaluation, selection, and calibration, pp 1–34
71. Yao YP, Hou W, Zhou AN (2009) UH model: three-dimensional unified hardening model for overconsolidated clays. Geotechnique 59(5):451–469
72. Zhang P, Yin ZY, Jin YF (2021) State-of-the-art review of machine learning applications in constitutive modeling of soils. Arch Comput Methods Eng 28(5):3661–3686
73. Zhou M, Shi Z, Peng C, Peng M, Cui KFE, Li B, Zhou GG (2024) Two-phase modelling of erosion and deposition process during overtopping failure of landslide dams using GPU-accelerated ED-SPH. Comput Geotech 166:105944
74. Anderson TB, Jackson R (1967) Fluid mechanical description of fluidized beds. Equations of motion. Industr Eng Chem Fundament 6(4):527–539
75. Chauchat J, Médale M (2010) A three-dimensional numerical model for incompressible two-phase flow of a granular bed submitted to a laminar shearing flow. Comput Methods Appl Mech Eng 199(9–12):439–449
76. Crowe CT, Schwarzkopf JD, Sommerfeld M, Tsuji Y (2011) Multiphase flows with droplets and particles
77. Crowe CT, Troutt TR, Chung J (1996) Numerical models for two-phase turbulent flows. Annu Rev Fluid Mech 28(1):11–43
78. Drew DA (1983) Mathematical modeling of two-phase flow. Annu Rev Fluid Mech 15(1):261–291
79. Elghobashi S (1994) On predicting particle-laden turbulent flows. Appl Sci Res 52:309–329
80. Hsu TJ, Liu PLF (2004) Toward modeling turbulent suspension of sand in the nearshore. J Geophys Res. https://doi.org/10.1029/2003JC002240
81. Ishii M (1975) Thermo-fluid dynamic theory of two-phase flow. NASA Sti/recon Tech Rep A 75:29657
82. Jiang F, Liu H, Chen X, Tsuji T (2022) A coupled LBM-DEM method for simulating the multiphase fluid-solid interaction problem. J Comput Phys 454:110963
83. Pudasaini SP, Fischer JT (2020) A mechanical erosion model for two-phase mass flows. Int J Multiph Flow 132:103416
84. Pudasaini SP, Mergili M (2019) A multi-phase mass flow model. J Geophys Res Earth Surf 124:2920–2942
85. Van Deemter JT, Van der Laan ET (1961) Momentum and energy balances for dispersed two-phase flow. Appl Sci Res 10:102–108
86. Vardoulakis I, Stavropoulou M, Papanastasiou P (1996) Hydromechanical aspects of the sand production problem. Transp Porous Media 22:225–244
87. Ouriemi M, Aussillous P, Guazzelli E (2009) Sediment dynamics. Part 1. Bed-load transport by laminar shearing flows. J Fluid Mech 636:295–319
88. Pudasaini SP (2012) A general two-phase debris flow model. J Geophys Res. https://doi.org/10.1029/2011JF002186
89. Pudasaini SP (2016) A novel description of fluid flow in porous and debris materials. Eng Geol 202:62–73
90. Lee CH, Low YM, Chiew YM (2016) Multi-dimensional rheology-based two-phase model for sediment transport and applications to sheet flow and pipeline scour. Phys Fluids. https://doi.org/10.1063/1.4948987
91. Mathieu A, Chauchat J, Bonamy C, Nagel T (2019) Two-phase flow simulation of tunnel and lee-wake erosion of scour below a submarine pipeline. Water 11(8):1727
92. Amoudry L, Hsu TJ, Liu PF (2008) Two-phase model for sand transport in sheet flow regime. J Geophys Res Oceans. https://doi.org/10.1029/2007JC004179C

93. Nagel T, Chauchat J, Bonamy C, Liu X, Cheng Z, Hsu TJ (2020) Three-dimensional scour simulations with a two-phase flow model. Adv Water Resour 138:103544
94. Tofany N, Wirahman T (2022) Numerical simulation of early stages of scour around a submarine pipeline using a two-phase flow model. Ocean Eng 264:112503
95. Biot MA (1941) General theory of three-dimensional consolidation. J Appl Phys 12:155–164
96. Cassel M, Lavé J, Recking A, Malavoi JR, Piégay H (2021) Bedload transport in rivers, size matters but so does shape. Sci Rep 11(1):508
97. Choi SU, Kwak S (2001) Theoretical and probabilistic analyses of incipient motion of sediment particles. KSCE J Civ Eng 5:59–65
98. Hu M, Wang Y, Li Y, Pang Z, Ren Y (2023) Development of drag force model for predicting the flow behavior of porous media based on genetic programming. Powder Technol 413:118041
99. Nasrollahi A, Neyshabouri AAS, Ahmadi G, Namin MM (2020) Numerical simulation of incipient particle motion. Int J Sedim Res 35(1):1–14
100. Singh UK, Ahmad Z, Kumar A, Pandey M (2019) Incipient motion for gravel particles in cohesionless sediment mixtures. Iran J Sci Technol Trans Civil Eng 43:253–262
101. Wang Y, Zhang G, Zhang J, Zhou S (2020) Characteristics of a bidirectional position of natural sediment on a two-dimensional river bed. Arab J Geosci 13:1–15
102. Yuan X, Ye F, Fu W, Wen L (2022) Estimating the critical shear stress for incipient particle motion of a cohesive soil slope. Sci Rep 12(1):9736
103. White CM (1940) The equilibrium of grains on the bed of a stream. Proc R Soc Lond A 174(958):322–338
104. Harris AR, Davidson CI (2008) Particle resuspension in turbulent flow: a stochastic model for individual soil grains. Aerosol Sci Technol 42(8):613–628
105. Egiazaroff IV (1965) Calculation of nonuniform sediment concentrations. J Hydraul Div 91(4):225–247
106. Hayashi T, Ozaki S, Ichibashi T (1980) Study on bed-load transport of sediment mixtures. In: Proceedings of the 24th Japanese Conference on Hydraulics
107. Soulsby RL (1997) Dynamics of marine sands: a manual for practical applications. Oceanogr Lit Rev 9(44):947
108. Wu W, Wang SS, Jia Y (2000) Nonuniform sediment transport in alluvial rivers. J Hydraul Res 38(6):427–434
109. Chiew YM, Parker G (1994) Incipient sediment motion on non-horizontal slopes. J Hydraul Res 32(5):649–660
110. Rehman K, Hong SH (2022) Influence of lateral flow contraction on bed shear stress estimation by using measured turbulent kinetic energy. Exp Thermal Fluid Sci 139:110742
111. Richardson JF, Zaki WN (1954) Sedimentation and fluidization. Part I. Trans Institut Chem Eng 32:35–53
112. Van Rijn LC (1987) Mathematical modelling of morphological processes in the case of suspended sediment transport; Delft Hydraulic. Laboratory: Delft, The Netherlands.
113. Wu W, Wang SS (2006) Formulas for sediment porosity and settling velocity. J Hydraul Eng 132(8):858–862
114. Zanke U (1977) Berechnung der sinkgeschwindigkeiten von sedimente. Mitt. Des Franzius_Instituts fuer Wasserbau, Heft 46, Seite 243, Technical University, Hannover
115. Zyserman JA, Fredsøe J (1994) Data analysis of bed concentration of suspended sediment. J Hydraul Eng 120(9):1021–1042
116. Mastbergen DR, Van Den Berg JH (2003) Breaching in fine sands and the generation of sustained turbidity currents in submarine canyons. Sedimentology 50(4):625–637
117. Partheniades E (1965) Erosion and deposition of cohesive soils. J Hydraul Div 91(1):105–139
118. Olsen NR, Melaaen MC (1993) Three-dimensional calculation of scour around cylinders. J Hydraul Eng 119(9):1048–1054
119. Olsen NR, Kjellesvig HM (1998) Three-dimensional numerical flow modeling for estimation of maximum local scour depth. J Hydraul Res 36(4):579–590
120. Roulund A, Sumer BM, Fredsøe J, Michelsen J (2005) Numerical and experimental investigation of flow and scour around a circular pile. J Fluid Mech 534:351–401
121. Liu X, García MH (2008) Three-dimensional numerical model with free water surface and mesh deformation for local sediment scour. J Waterw Port Coast Ocean Eng 134(4):203–217
122. Gothel O (2008) Numerical modeling of flow and wave-induced scour around vertical structures (PhD thesis). Leibniz University of Hanover, Faculty of Civil Engineering and Geodesy, Hanover
123. Khosronejad A, Kang S, Borazjani I, Sotiropoulos F (2011) Curvilinear immersed boundary method for simulating coupled flow and bed morphodynamic interactions due to sediment transport phenomena. Adv Water Resour 34(7):829–843
124. Baranya S, Olsen NRB, Stoesser T, Sturm T (2012) Three-dimensional RANS modeling of flow around circular piers using nested grids. Eng Appl Comput Fluid Mech 6(4):648–662
125. Stahlmann A (2014) Numerical and experimental modeling of scour at foundation structures for offshore wind turbines. In ISOPE International Ocean and Polar Engineering Conference (pp. ISOPE-I). ISOPE
126. Baykal C, Sumer BM, Fuhrman DR, Jacobsen NG, Fredsøe J (2017) Numerical simulation of scour and backfilling processes around a circular pile in waves. Coast Eng 122:87–107
127. Xu J, Xia J, Wang L, Avital EJ, Zhu H, Wang YM (2022) An improved Eulerian method in three-dimensional direct numerical simulation on the local scour around a cylinder. Appl Math Model 110:320–337
128. Liang D, Cheng L, Li F (2005) Numerical modeling of flow and scour below a pipeline in currents: Part II. Scour Simulat Coastal Eng 52(1):43–62
129. Burkow M, Griebel M (2016) A full three dimensional numerical simulation of the sediment transport and the scouring at a rectangular obstacle. Comput Fluids 125:1–10
130. Fan F, Liang B, Bai Y, Zhu Z, Zhu Y (2017) Numerical modeling of local scour around hydraulic structure in sandy beds by dynamic mesh method. J Ocean Univ China 16:738–746
131. Belytschko T, Liu WK, Moran B, Elkhodary K (2014) Nonlinear finite elements for continua and structures
132. Liu WK, Li S, Park HS (2022) Eighty years of the finite element method: birth, evolution, and future. Arch Comput Methods Eng 29(6):4431–4453
133. Logan DL (2002) A first course in the finite element method
134. Zienkiewicz OC, Taylor RL (2005) The finite element method for solid and structural mechanics
135. Feng H, Huang M, Shi Z, Shen K, Wang B (2024) Macro-element modeling of suction caisson subjected to vertical tensile loading via up-scaling soil stress-strain relations. Ocean Eng 304:117850
136. Huang M, Feng H, Shi Z, Shen K, Wang B (2024) Inferred Winkler model for uplift response of suction caisson in undrained clays. Acta Geotech 19(1):437–454
137. Zhang MH, Yin ZY, Fu Y (2023) Numerical investigation of pull-out capacity and failure mechanism of suction anchors with mooring line in sand. Ocean Eng 280:114837
138. Arnold DN, Brezzi F, Fortin M (1984) A stable finite element for the stokes equations. Calcolo 21(4):337–344
139. Donea J, Huerta A (2003) Finite element methods for flow problems

140. Hughes TJ, Franca LP, Balestra M (1986) A new finite element formulation for computational fluid dynamics: V. Circumventing the Babuška-Brezzi condition: A stable Petrov-Galerkin formulation of the Stokes problem accommodating equal-order interpolations. Comput Methods App Mech Eng 59(1):85–99
141. Lewis RW, Nithiarasu P, Seetharamu KN (2004) Fundamentals of the finite element method for heat and fluid flow
142. Raptis A, Kyriakoudi K, Xenos MA (2019) Finite element analysis in fluid mechanics. Mathematical analysis and applications. Springer International Publishing, Cham, pp 481–510
143. Zienkiewicz OC, Taylor RL, Nithiarasu P (2013) The finite element method for fluid dynamics
144. Brooks AN, Hughes TJ (1982) Streamline upwind/Petrov-Galerkin formulations for convection dominated flows with particular emphasis on the incompressible Navier-Stokes equations. Comput Methods Appl Mech Eng 32(1–3):199–259
145. Fuhrman DR, Baykal C, Sumer BM, Jacobsen NG, Fredsøe J (2014) Numerical simulation of wave-induced scour and backfilling processes beneath submarine pipelines. Coast Eng 94:10–22
146. Dyer KR (1995) Sediment transport processes in estuaries
147. Cremonesi M, Franci A, Idelsohn S, Oñate E (2020) A state of the art review of the particle finite element method (PFEM). Arch Comput Methods Eng 27:1709–1735
148. Idelsohn SR, Oñate E, Pin FD (2004) The particle finite element method: a powerful tool to solve incompressible flows with free-surfaces and breaking waves. Int J Numer Meth Eng 61(7):964–989
149. Idelsohn SR, Oñate E, Del Pin F, Calvo N (2006) Fluid-structure interaction using the particle finite element method. Comput Methods Appl Mech Eng 195(17–18):2100–2123
150. Galano N, Moreno-Casas PA, Abell JA (2021) Extending the particle finite element method for sediment transport simulation. Comput Methods Appl Mech Eng 380:113772
151. Zhu M, Scott MH (2014) Improved fractional step method for simulating fluid-structure interaction using the PFEM. Int J Numer Meth Eng 99(12):925–944
152. Zhu M, Scott MH (2014) Modeling fluid–structure interaction by the particle finite element method in OpenSees. Comput Struct 132:12–21
153. Oñate E, Celigueta MA, Idelsohn SR, Salazar F, Suárez B (2011) Possibilities of the particle finite element method for fluid-soil-structure interaction problems. Comput Mech 48:307–318
154. Mast CM (2013) Modeling landslide-induced flow interactions with structures using the material point method (Doctoral dissertation)
155. Zhang HW, Wang KP, Chen Z (2009) Material point method for dynamic analysis of saturated porous media under external contact/impact of solid bodies. Comput Methods Appl Mech Eng 198(17–20):1456–1472
156. Zabala F, Alonso EE (2011) Progressive failure of Aznalc´ollar dam using the material point method. Geotechnique 61(9):795–808
157. Jassim I, Stolle D, Vermeer P (2013) Two-phase dynamic analysis by material point method. Int J Numer Anal Meth Geomech 37(15):2502–2522
158. Yerro A, Alonso EE, Pinyol NM (2015) The material point method for unsaturated soils. Geotechnique 65(3):201–217
159. Ceccato F, Yerro A, Girardi V, Simonini P (2021) Two-phase dynamic MPM formulation for unsaturated soil. Comput Geotech 129:103876
160. Abe K, Soga K, Bandara S (2014) Material point method for coupled hydromechanical problems. J Geotech Geoenviron Eng 140(3):04013033
161. Bandara S, Soga K (2015) Coupling of soil deformation and pore fluid flow using material point method. Comput Geotech 63:199–214
162. Liang D, Zhao X, Soga K (2020) Simulation of overtopping and seepage induced dike failure using two-point MPM. Soils Found 60(4):978–988
163. Zhao KL, Qiu LC, Yuan TJ, Wang Y, Liu Y (2023) Two-Phase MPM simulation of surge waves generated by a granular landslide on an erodible slope. Water 15(7):1307
164. Zhao Y, Zhou ZQ, Bi J, Wang CL, Wu ZJ (2023) Numerical simulation the fracture of rock in the framework of plastic-bond-based SPH and its applications. Comput Geotech 157:105359
165. Feng K, Huang D, Wang G (2021) Two-layer material point method for modeling soil–water interaction in unsaturated soils and rainfall-induced slope failure. Acta Geotech 16(8):2529–2551
166. Liang D, Zhao X, Martinelli M (2017) MPM simulations of the interaction between water jet and soil bed. Procedia Eng 175:242–249
167. Yang YS, Yang TT, Qiu LC, Han Y (2019) Simulating the overtopping failure of homogeneous embankment by a Double-Point Two-Phase MPM. Water 11(8):1636
168. Zhao X (2019) Improvements of MPM and Its Applications in Modelling Rapid Soil/Water Movements (Doctoral dissertation, University of Cambridge)
169. Gingold RA, Monaghan JJ (1977) Smoothed particle hydrodynamics: theory and application to non-spherical stars. Mon Not R Astron Soc 181(3):375–389
170. Crespo AJC, Domínguez JM, Rogers BD, Gómez-Gesteira M, Longshaw S, Canelas R, Vacondio R, Barreiro A, García-Feal O (2015) DualSPHysics: open-source parallel CFD solver based on Smoothed Particle Hydrodynamics (SPH). Comput Phys Commun 187:204–216
171. Hammani I, Marrone S, Colagrossib A, Oger G, Le Touz´e, D., (2020) Detailed study on the extension of the δ-SPH model to multi-phase flow. Comput Methods Appl Mech Engrg 368:113189
172. Bui HH, Fukagawa R, Sako K, Ohno S (2008) Lagrangian meshfree particles method (SPH) for large deformation and failure flows of geomaterial using elastic–plastic soil constitutive model. Int J Numer Anal Meth Geomech 32(12):1537–1570
173. Bui HH, Nguyen GD (2021) Smoothed particle hydrodynamics (SPH) and its applications in geomechanics: From solid fracture to granular behaviour and multiphase flows in porous media. Comput Geotech 138:104315
174. Peng C, Bašić M, Blagojević B, Bašić J, Wu W (2021) A Lagrangian differencing dynamics method for granular flow modeling. Comput Geotech 137:104297
175. Peng C, Wang S, Wu W, Yu HS, Wang C, Chen JY (2019) LOQUAT: an open-source GPU-accelerated SPH solver for geotechnical modeling. Acta Geotech 14:1269–1287
176. Fourtakas G, Rogers BD (2016) Modelling multi-phase liquid-sediment scour and resuspension induced by rapid flows using Smoothed Particle Hydrodynamics (SPH) accelerated with a Graphics Processing Unit (GPU). Adv Water Resour 92:186–199
177. Jilani AN, Hashemi SU (2013) Numerical investigations on bed load sediment transportation using SPH method. Scientia Iranica 20(2):294–299
178. Zubeldia EH, Fourtakas G, Rogers BD, Farias MM (2018) Multi-phase SPH model for simulation of erosion and scouring by means of the shields and Drucker-Prager criteria. Adv Water Resour 117:98–114
179. Drucker DC, Prager W (1952) Soil mechanics and plastic analysis for limit design. Q Appl Math 10(2):157–165
180. Baumgarten AS, Couchman BL, Kamrin K (2021) A coupled finite volume and material point method for two-phase simulation of liquid–sediment and gas–sediment flows. Comput Methods Appl Mech Eng 384:113940

181. Tran QA, Grimstad G, Ghoreishian Amiri S, A. (2024) MPMICE: A hybrid MPM-CFD model for simulating coupled problems in porous media. Application to earthquake-induced submarine landslides. Int J Num Methods Eng 125(5):e7383
182. Wang Z, Wang G (2023) A coupled MPM and CBFEM framework for large deformation simulation of porous media interacting with pore and free fluid. Comput Geotech 163:105746
183. Pan S, Yamaguchi Y, Suppasri A, Moriguchi S, Terada K (2021) MPM-FEM hybrid method for granular mass–water interaction problems. Comput Mech 68(1):155–173
184. Zhu Y, Ishikawa T, Zhang Y, Nguyen BT, Subramanian SS (2022) A FEM-MPM hybrid coupled framework based on local shear strength method for simulating rainfall/runoff-induced landslide runout. Landslides 19(8):2021–2032
185. Lee K, Jeong S (2018) Large deformation FE analysis of a debris flow with entrainment of the soil layer. Comput Geotech 96:258–268
186. Jeong S, Lee K (2019) Analysis of the impact force of debris flows on a check dam by using a coupled Eulerian-Lagrangian (CEL) method. Comput Geotech 116:103214
187. Lee K, Kim Y, Ko J, Jeong S (2019) A study on the debris flow-induced impact force on check dam with-and without-entrainment. Comput Geotech 113:103104
188. Ahmadzadeh M, Saranjam B, Fard AH, Binesh AR (2014) Numerical simulation of sphere water entry problem using Eulerian-Lagrangian method. Appl Math Model 38(5–6):1673–1684
189. Arena G, Groh R, Theunissen R, Weaver P, Pirrera A (2016) Adaptive nonlinear structures for flow regulation: modelling fluid-structure interactions with coupled eulerian-lagrangian meshes. In 2016 SIMULIA Regional User Meeting
190. Qiu G, Henke S, Grabe J (2011) Application of a Coupled Eulerian-Lagrangian approach on geomechanical problems involving large deformations. Comput Geotech 38(1):30–39
191. Zhao M, Cheng L, Zang Z (2010) Experimental and numerical investigation of local scour around a submerged vertical circular cylinder in steady currents. Coast Eng 57(8):709–721
192. Chen HH (2019) Experimental study of scour around monopile and jacket-type offshore wind turbine foundations. J Mar Sci Technol 27(2):2
193. Jackson D, Short A (2020) Sandy beach morphodynamics
194. Amini A, Melville BW, Ali TM, Ghazali AH (2012) Clear-water local scour around pile groups in shallow-water flow. J Hydraul Eng 138(2):177–185
195. Xiong L, Yang J, Tian X (2017) Influence of a Seabed Trench on a Taut Mooring Line. In: International Conference on Offshore Mechanics and Arctic Engineering (Vol. 57632, p. V001T01A031). American Society of Mechanical Engineers
196. Reeks MW, McKee S (1984) The dispersive effects of Basset history forces on particle motion in a turbulent flow. The Physics of Fluids 27(7):1573–1582
197. Saffman PG (1965) The lift on a small sphere in a slow shear flow. J Fluid Mech 22(2):385–400
198. Rijn LCV (1984) Sediment transport, part II: suspended load transport. J Hydraul Eng 110(11):1613–1641
199. Mitchener H, Torfs H (1996) Erosion of mud/sand mixtures. Coast Eng 29(1–2):1–25
200. Hager WH, Oliveto G (2002) Shields' entrainment criterion in bridge hydraulics. J Hydraul Eng 128(5):538–542
201. Annandale GW (2006) Scour technology-mechanics and engineering practice. McGraw-Hill, New York
202. Chang DS, Zhang LM (2011) A stress-controlled erosion apparatus for studying internal erosion in soils. Geotech Testing J 34(6):579–589
203. Einstein HA (1942) Formulas for the transportation of bed load. Transactions 2140:561–597
204. Meyer-Peter E, Müller R (1948) Formulas for bed-load transport. Report of 2nd Meeting of the International Association of Hydraulic and Structural Research, pp 34–64
205. Einstein HA (1950) The bed-load function for sediment transportation in open channel flows (No. 1026). US Department of Agriculture
206. Bagnold RA (1956) The flow of cohesionless grains in fluids. Philosophical Transactions of the Royal Society of London. Ser A Mathemat Phys Sci 249(964):235–297
207. Yalin MS (1963) An expression for bed-load transportation. J Hydraul Div 89(3):221–250
208. Wong M, Parker G (2006) Reanalysis and correction of bed-load relation of Meyer-Peter and Müller using their own database. J Hydraul Eng 132(11):1159–1168